Politecnico di Torino

Mechatronic Engineering
A.a. 2025/2026
Graduation Session March 2026

Development of Simplified Modeling Approaches for Performance Predictions of Axial Flux PM Machines

Supervisors:
Federica Graffeo
Silvio Vaschetto
Fabio Venturini
Matias Sebastian Jimenez Molina

Candidate:
Francesco Cusato

Abstract

Axial Flux Permanent Magnet (AFPM) machines have attracted significant interest in the field of electric traction due to their high torque and power density, compact structure, and suitability for direct-drive applications.

This thesis addresses both the preliminary design and the performance prediction of AFPM machines. In particular, an analytical electromagnetic sizing methodology is employed to determine the main machine dimensions and equivalent-circuit parameters starting from target performance specifications, material properties, and electromagnetic loading constraints.

Nevertheless, accurate performance prediction of AFPM machines typically requires high-fidelity simulation techniques, such as three-dimensional Finite Element Analysis (3D FEA), which are computationally expensive and time-consuming. Such methods are not always practical during the early design stages or when rapid optimization is required.

For this reason, simplified modeling approaches are investigated and validated in order to evaluate the electromagnetic performance of the sized machine with reduced computational effort. Two modeling approaches are considered. The first is a two-dimensional Finite Element Modelling approach, specifically the Linear Motor Modelling Approach (LMMA), in which the AFPM machine is represented through an equivalent planar geometry. The second approach is a quasi-three-dimensional (2.5D) modelling strategy, which extends the 2D formulation by evaluating multiple radial slices of the machine and computing global quantities through an averaging process over the considered radii. Each approach is parameterized using machine geometry and material properties and is benchmarked against a high-fidelity 3D FEA reference model.

The comparison with the 3D reference model allows the validation of the simplified modelling approaches and highlights their capability to reproduce the main electromagnetic behaviour of the machine. The study therefore demonstrates the suitability of simplified models for the preliminary analysis and performance evaluation of AFPM machines.

Table of Contents

Introduction 1

1 Overview of electric machine topologies 3
- 1.1 Electric Machines 3
  - 1.1.1 Background and Typologies 3
- 1.2 Axial and Radial Flux Machines 5

2 Axial Flux Permanent Magnet Machines 7
- 2.1 Description and Operating Principle 7
- 2.2 Topologies 8
  - 2.2.1 Single-stator/Single-rotor SSSR 9
  - 2.2.2 Double-stators/Single-rotor DSSR 10
  - 2.2.3 Single-stator/Double-rotors SSDR 11
  - 2.2.4 Multi-stator/Multi-rotor MSMR 14
- 2.3 Structural Configuration of AFPM Machines 14
  - 2.3.1 Influence of Materials on Performance 14
  - 2.3.2 Winding Configurations and Design Considerations 15

3 Sizing Procedure 17
- 3.1 User Inputs and Sizing Procedure 17
  - 3.1.1 Input Parameters 18
  - 3.1.2 Design Assumptions 20
- 3.2 Preliminary Calculations 20
- 3.3 Magnetic Core Sizing 23
  - 3.3.1 Step 1: Geometry initialization and diameters 23
  - 3.3.2 Step 2: Yoke and tooth sizing 24
  - 3.3.3 Step 3: Torque, useful slot area, and linear current density . 25
  - 3.3.4 Step 4: Stopping criterion 26
- 3.4 Circuit Parameters Calculation 26
  - 3.4.1 Phase resistance 27
  - 3.4.2 Inductance calculation 28

3.4.3 Conductors in series per phase 29
3.5 Case Study 30
3.5.1 Design Targets and Rated Operating Point 31
3.5.2 Sizing Input Parameters 32
3.5.3 Sizing Results 32

4 2D and Q-3D approaches 35
4.1 2D Finite Element Modelling Approaches 35
4.1.1 Reduction from 3D to 2D models 35
4.1.2 Equivalent 2D modelling approaches 37
4.2 Quasi-3D approach 38
4.3 Comparison of Computational Efficiency 40
4.4 Discussion 40
4.4.1 Concluding Remarks 41

5 FEMM Models 42
5.1 MATLAB–FEMM workflow and simulation driver 42
5.1.1 Input data and parameterization 42
5.1.2 Simulation settings 43
5.1.3 Full vs periodic-sector model 43
5.1.4 Operating mode selection: no-load vs on-load 44
5.1.5 Structured interface to FEMM routines 45
5.2 Sector-based FEMM model generation and simulation (`femm_afpm_flex`) 45
5.2.1 FEMM initialization and material setup 46
5.2.2 Admissible periodicity and boundary mode selection 46
5.2.3 Geometrical mapping to a planar tangential domain 47
5.2.4 Automated construction of rotor, magnets, air gap and stator 47
5.2.5 Boundary conditions: lateral symmetry and Dirichlet closure 48
5.2.6 Air gap slicing and “moving band” emulation 48
5.2.7 Simulation timeline and rotor position sampling 49
5.2.8 Post-processing: flux linkage, back-EMF, and torque 49
5.2.9 Electrical angle identification from no-load flux linkage . . . 51
5.2.10 Exported data 52
5.2.11 No-load results: flux density map, flux linkage and back-EMF 52
5.2.12 On-load results: current excitation and electromagnetic torque 55
5.3 From 2D mean-radius model to quasi-3D averaging 56

6 Comparison between 2D, Q-3D and 3D FEM Models 58
6.1 Overview of the comparison methodology 58
6.2 Two-dimensional and quasi-3D model reference 59
6.3 Three-dimensional model reference 60

6.4 Air gap flux density comparison 61
6.5 No-load flux linkage 62
6.6 Back-EMF comparison 63
6.7 Electromagnetic torque comparison 64
6.8 Discussion and modelling trade-offs 65

7 Conclusion 66

A MATLAB Implementation 69

B FEMM Implementation 79

C FEMM Implementation Details 85
C.1 Periodicity handling 85
C.2 Precompute dimensions 86
C.3 Air gap moving band 86
C.4 Current excitation: load vs no-load 88
C.5 Solve and post-processing 89
C.6 d–q axis alignment 90

Bibliography 91

List of Symbols and Abbreviations

Abbreviations

2.5D	Quasi-Three-Dimensional
2D	Two-Dimensional
3D	Three-Dimensional
abc	Three-phase reference frame
AC	Alternating Current
AF	Axial Flux
AFM	Axial Flux Machine
AFPM	Axial Flux Permanent Magnet
AF-SPM	Axial Flux Surface Mounted Permanent Magnet
BC	Boundary Condition
BLDC	Brushless Direct Current
DC	Direct Current
dq	Rotating reference frame (direct–quadrature axes)
DSSR	Double-Stator Single-Rotor
DW	Distributed Winding
EMF	Electromotive Force
FEA	Finite Element Analysis
FEM	Finite Element Method
FEMM	Finite Element Method Magnetics
FSCW	Fractional-Slot Concentrated Winding
IRMA	Inner Radius Modelling Approach
LMMA	Linear Motor Modelling Approach
MSMR	Multi-Stator Multi-Rotor
ORMA	Outer Radius Modelling Approach
PM	Permanent Magnet
Q-3D	Quasi-Three-Dimensional

RF	Radial Flux
RFPM	Radial Flux Permanent Magnet
SMC	Soft Magnetic Composite
SSDR	Single-Stator Double-Rotor
SSSR	Single-Stator Single-Rotor

Symbols

A_{cu}	Effective copper area
A_{us}	Useful slot area
B_g	Average air-gap flux density [T]
B_{g1}	Fundamental component of the air-gap flux density [T]
B_r	PM remanent flux density [T]
B_{ts}	Maximum tooth flux density [T]
B_{ys}	Maximum stator yoke flux density [T]
B_{yr}	Maximum rotor yoke flux density [T]
D_1	Inner lamination diameter
D_2	Outer lamination diameter
D_{ag}	Average air-gap diameter
D_{avg}	Average diameter
D_e	Auxiliary diameter
D_i	Mechanical inner diameter
D_m	Average diameter
D_{sh}	Shaft diameter
D_{slc}	Equivalent diameter of slice slc
E_0	No-load back-EMF magnitude
E_p	Peak back-EMF
f_r	Rated frequency
h_{gap}	Air-gap thickness
h'_{gap}	Carter-corrected air-gap thickness
h_{pm}	PM axial thickness
h'_{pm}	Equivalent magnet thickness
h_{us}	Useful slot height
h_{ys}	Stator yoke height
h_{yr}	Rotor yoke height
H_c	Coercive field
I_d	d-axis current
I_q	q-axis current

I_s	Rated phase current
J_{rms}	RMS slot current density
K_C	Carter's coefficient
K_E	Derived constant in $E_0 = K_E Z_{ph}$
K_I	Derived constant in $I_s = K_I / Z_{ph}$
K_L	Derived constant in $L_{sync} = K_L Z_{ph}^2$
K_R	Derived constant in $R_s = K_R Z_{ph}^2$
K_s	Linear current density
$K_{s,\max}$	Maximum admissible linear current density
k_1	Correction factor for slot-sharing phases
k_{cu}	Copper fill factor
k_{fe}	Lamination stacking factor
k_{w1}	Fundamental winding factor
k_{ws}	Winding factor
l_{core}	Core radial length
$l_{ew,ave}$	Average end-winding length
l_{PM}	PM radial length
l_{slot}	Slot length
$l_{turn,ave}$	Average turn length
L_c	Axial core length
L_{end}	End-winding leakage inductance
L_{gap}	Air-gap leakage inductance
L_m	Magnetizing inductance
L_{slot}	Slot leakage inductance
L_{sync}	Synchronous inductance
L_{tt}	Tooth-tip leakage inductance
M_{elec}	Number of electrical periods simulated
μ_0	Permeability of free space
μ_{env}	Relative permeability of end-winding environment
μ_r	PM relative permeability
n_r	Rated speed
n_{sectors}	Number of angular sectors
n_{slc}	Number of radial slices
n_{sr}	Winding pitch reduction factor
N_1	Number of simulated points
N_s	Number of stator slots
N_{turns}	Turns per slot
p	Pole pairs
q	Slots per pole per phase
R_s	Phase resistance
ρ_{cu}	Copper resistivity

σ_{gap}	Air-gap leakage factor
slc	Slice index
t_k	Discrete time instant
T_e	Instantaneous electromagnetic torque
T_{ave}	Mean torque
T_{em}	Electromagnetic torque
T_p	Peak torque
T_r	Rated torque
T_{mean}	Mean electromagnetic torque
T_{ref}	Reference torque
τ_p	Pole pitch
τ_s	Slot pitch
V_p	Peak back-EMF
V_r	Rated phase voltage
w_s	Slot width
w_{t1}	Inner tooth width
w_{t2}	Outer tooth width
Z_{ph}	Conductors in series per phase
α_{pm}	Magnet pole-arc ratio
β_{ax}	Angular winding parameter
Δt	Time step
$\Delta\theta_{\text{mech}}$	Mechanical angular step
$\Delta\theta_{\text{mech,tot}}$	Total simulated mechanical span
λ_1	Slot leakage permeance factor
λ_2	Slot leakage permeance factor
λ_{12}	Slot leakage permeance factor
λ_{AFM}	Aspect ratio $\left(\frac{D_1}{D_2}\right)$
λ_A	Phase-A flux linkage
λ_B	Phase-B flux linkage
λ_C	Phase-C flux linkage
λ_p	Peak flux linkage
λ_{slot}	Slot leakage permeance factor
λ_{tt}	Tooth-tip leakage permeance factor
ω_e	Electrical angular frequency
ω_m	Mechanical angular speed
θ_e	Electrical angle
θ_{e0}	Electrical alignment angle
θ_m	Mechanical rotor position
θ_{m0}	Mechanical alignment angle
θ_0	Electrical angle offset
TR_{pp}	Peak-to-peak torque ripple

Introduction

The increasing demand for sustainable and efficient transportation has accelerated the global transition towards electric mobility. A critical enabler of this transition is the development of high-performance electric machines that combine compactness, efficiency, and reliability. Among the different machine topologies, Axial Flux Permanent Magnet (AFPM) machines have gained particular attention due to their distinctive advantages: reduced axial length, high torque and ease of integration in wheel-hub and compact drivetrains. These features make AFPM machines strong candidates for automotive traction applications, aerospace applications, and renewable energy systems.

While AFPM machines offer considerable benefits, their electromagnetic behavior is complex, largely due to three-dimensional flux paths, fringing effects, and the influence of winding and geometry variations. As a result, high-fidelity simulation methods, particularly 3D Finite Element Analysis (FEA), are commonly used for performance prediction. However, the computational burden of such methods limits their practicality in early design exploration, rapid prototyping, and optimization loops where a large number of iterations are required.

This challenge motivates the need for simplified modeling approaches, which, although less detailed than full FEA, can capture the essential physics of AFPM operation with sufficient accuracy at a fraction of the computational cost. Such approaches are especially valuable in the pre-dimensioning phase, where fast evaluations guide design decisions.

The aim of this thesis is to develop and investigate an analytical sizing methodology and simplified modeling approaches for Axial Flux Permanent Magnet (AFPM) machines. The proposed work therefore focuses on two complementary aspects: the preliminary electromagnetic dimensioning of the machine, based on the analytical framework presented in [1], and the development of reduced-order modeling strategies for performance prediction. In particular, two simplified modeling approaches are considered: a two-dimensional (2D) modeling approach and a quasi-three-dimensional (2.5D) approach, following the methodologies discussed in [2].

Within the 2D framework, three different modeling formulations can be identified:

1. Linear Motor Modelling Approach (LMMA).

2. Inner Radius Modelling Approach (IRMA).
3. Outer Radius Modelling Approach (ORMA).

Among these, only the LMMA model is considered and developed in detail within this thesis, while the remaining formulations are introduced for completeness and discussed more in a dedicated chapter.

The quasi-3D approach builds upon the 2D formulation by evaluating the machine behavior at multiple radial slices and deriving global quantities through an averaging procedure. Both the 2D and the quasi-3D LMMA are implemented and parameterized. The evaluation criteria include prediction accuracy, computational cost, and applicability during different design phases.

The thesis is organized as follows. Chapter 1 reviews the electromagnetic background. Chapter 2 introduces AFPM machines and their main topologies. Chapter 3 presents the sizing methodology. Chapter 4 discusses simplified and quasi-3D modeling approaches. Chapter 5 describes the implementation of the FEMM-based models. Chapter 6 presents a comparative analysis between the 2D, quasi-3D, and 3D reference results. Finally, Chapter 7 concludes the thesis and outlines directions for future work.

Chapter 1

Overview of electric machine topologies

1.1 Electric Machines

The discussion begins with a general overview of the most common categories of electric machines used in modern engineering applications. Afterwards, attention will be directed specifically to the AFM family, with emphasis on their structural features, operational benefits, and inherent limitations.

The aim of this chapter is not to provide an exhaustive treatment of electric machines as a whole, given the breadth of the topic, but rather to establish a clear context for Axial Flux Machines. Particular focus is placed on the reasons why they represent a valid alternative to conventional Radial Flux Machines and on the factors that continue to drive research interest in this technology.

1.1.1 Background and Typologies

Electric machines are devices capable of converting electrical energy into mechanical energy and vice versa [3]. In AC machines, the rotating magnetic field is produced by currents injected into the stator windings, while the rotor excitation depends on the machine type. For instance, permanent magnet machines use rotor-mounted magnets, whereas induction machines rely on currents induced in the rotor conductors.

Many electrical machines are reversible energy conversion devices and can operate either as a **motor** or as a **generator**, depending on the direction of power flow.

When electrical power is supplied to the machine and converted into mechanical output power, it operates as a **motor**. Conversely, when mechanical power is provided at the shaft and converted into electrical power, the same device operates as a **generator**.

In this thesis, the analysis focuses on motor operation, i.e., on electrically supplied machines delivering mechanical torque and power.

Although sometimes regarded as a relatively recent innovation in traction applications, electric motors are in fact extensively used in almost every industrial sector. They play a crucial role in vehicles, machines, and industrial systems, where they combine high specific performance and excellent energy conversion efficiency with good reliability and reduced environmental impact.

The main parts of an electric motor are the **rotor** and the **stator**. The rotor represents the moving component, generally cylindrical and connected to the drive shaft. The stator, on the other hand, is fixed and is responsible for generating the magnetic field that interacts with the rotor field to produce the desired torque. These fundamental principles will be explained in the following chapters.

Below, the main categories of electric motors are summarized:

- **Direct Current (DC) motors**: powered by a constant voltage source, such as a battery. Historically relevant for their simple torque control. However, the presence of mechanical commutators limits reliability and high-speed operation, making them less suitable for modern high-performance applications.

- **Alternating Current (AC) motors**: powered by an alternating voltage, typically single-phase, three-phase, or, in advanced applications, multiphase.

    - **Asynchronous (induction) motors** [4]: the most common type of AC motor. The rotor speed is lower than the synchronous speed of the stator field, with rotor currents induced by relative motion. They are simple, rugged, and economical, widely used in industrial applications.

    - **Synchronous motors** [4]: characterized by a rotor speed equal to the synchronous speed of the stator magnetic field. They can be classified according to their excitation method:

        - **Permanent Magnet Synchronous Motors (PMSMs)**: the rotor field is generated by permanent magnets. They are characterized by high efficiency and high torque density. According to magnet placement, they can be further divided into:
            - Surface-mounted Permanent Magnet (SPM)
            - Interior Permanent Magnet (IPM)
        - **Wound-field synchronous motors**: the rotor magnetic field is generated by DC excitation windings. They allow a sharper field control but introduce additional rotor losses and increased structural complexity.

- **Synchronous Reluctance Motors (SynRM)**: torque is produced by rotor saliency and magnetic reluctance variation, without permanent magnets or rotor windings.
- **Switched Reluctance Motors (SRM)**: characterized by doubly-salient structure and concentrated windings. Torque is produced through sequential phase excitation and strong reluctance variation.

1.2 Axial and Radial Flux Machines

Electric machines can also be classified according to the orientation of the magnetic flux in the air gap. The two main categories are **Radial Flux (RF)** and **Axial Flux (AF)** machines.

In RF machines, the magnetic flux is directed **radially**, i.e., perpendicular to the shaft axis. In AF machines, by contrast, the flux is oriented **axially**, namely parallel to the shaft axis, Fig. 1.1 and Fig. 1.2 shown a schematic view of the two machine topologies. This topological difference significantly affects the geometrical layout of the machine, the scaling of torque production, and the distribution of electromagnetic forces.

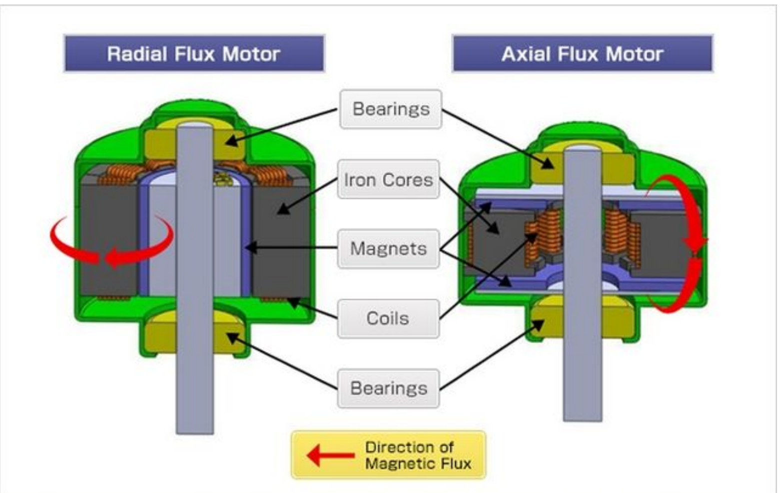

Figure 1.1: Direction of the magnetic flux in radial and axial flux machines.

In RF machines, the cylindrical geometry naturally leads to a relatively high aspect ratio, defined as the ratio between the active axial length and the machine diameter. Torque production is mainly associated with the axial active length and air-gap radius.

In contrast, AF machines typically exhibit a disc-like geometry with a low aspect ratio. In this case, torque production is predominantly linked to the machine outer diameter.

Figure 1.2 highlights the geometric difference between cylindrical RF machines and disc-type AF machines, emphasizing the variation in aspect ratio and active torque-producing surface.

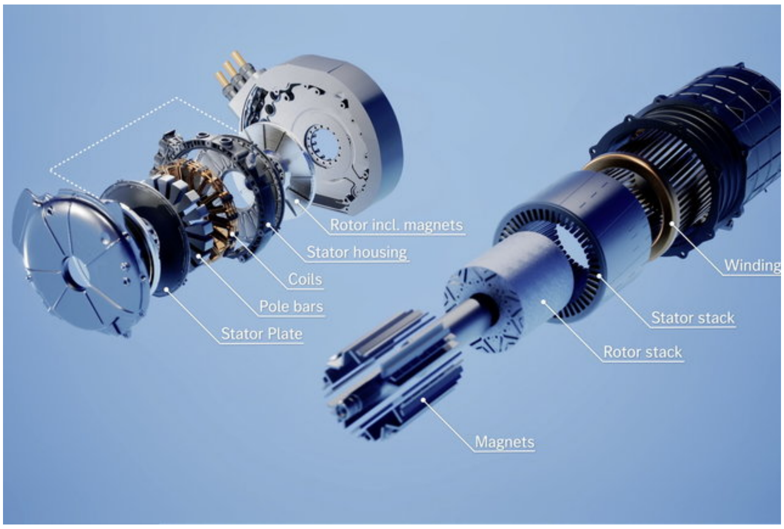

Figure 1.2: Geometrical comparison between radial and axial flux machines.

Despite these geometrical differences, AF and RF machines share the same fundamental electromagnetic operating principles and control strategies. The distinction concerns the spatial arrangement of the magnetic circuit rather than the energy conversion mechanism itself.

However, in single-sided AF machines the axial orientation of the flux can generate significant **axial magnetic forces** due to the normal component of the air-gap flux density. These forces tend to attract rotor and stator toward each other and must be carefully considered in the mechanical design. In practice, most commercial AF machines adopt double-sided topologies in which these axial forces are largely balanced.In RF machines, the magnetic flux is mainly oriented in the radial direction. As a result, the electromagnetic forces are predominantly radial rather than axial [3].

From a performance perspective, AF machines offer advantages in terms of **torque density and compact axial dimensions**. Nevertheless, their discoidal geometry introduces additional mechanical and manufacturing challenges, which partly explain the predominance of RF machines in industrial production [5].

Chapter 2

Axial Flux Permanent Magnet Machines

Having introduced the general background on electric machines in Chapter 1, this chapter focuses specifically on **Axial Flux Permanent Magnet (AFPM) machines**. The chapter begins with a description of their main characteristics and operating principle, underlining the aspects that distinguish them from conventional radial flux machines. Subsequently, the principal **AFPM topologies** are presented, highlighting their specific features and fields of application. Finally, the structural configuration of the **stator and rotor** is analyzed, with particular attention to their design, materials, and influence on the overall performance of the machine.

2.1 Description and Operating Principle

Axial flux electric machines, also referred to as **disc-type machines**, represent a specific electromagnetic topology in which the magnetic flux predominantly closes along the axial direction, rather than radially as in conventional radial flux machines.

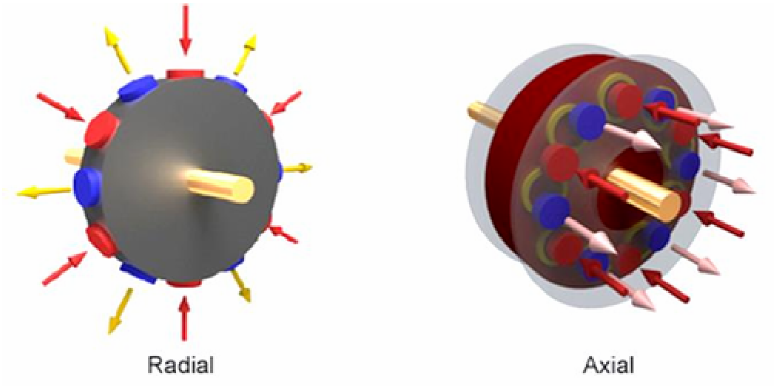

Figure 2.1: Flux in axial and radial machines

The axial flux configuration refers to the geometric arrangement of the magnetic circuit and can be applied to different types of electrical machines, including permanent magnet, induction, and reluctance machines.

In this thesis, the focus is placed on **Axial Flux Surface Mounted Permanent Magnet (AF-SPM) machines**, which combine the axial magnetic flux topology with permanent magnet excitation.

Compared to other excitation methods, permanent magnet machines are particularly suited for electric traction applications due to their high efficiency, high torque density.

As shown in Fig. 2.1, in a radial flux motor the magnetic flux is oriented radially, whereas in an axial flux motor the flux is directed parallel to the shaft axis.

These machines naturally find application in the **automotive sector**, where high torque density and compactness are key requirements. Multi-stage configurations, consisting of multiple stators and rotors, can be developed to increase the effective torque-producing surface, further enhancing torque density.

2.2 Topologies

According to the number of stators and rotors, AFPM machines can generally be classified into four categories [6], illustrated in Figure 2.2:

- **Single-stator / Single-rotor (SSSR)** Compact structure and high torque capacity make this topology widely used in servo drives and transportation. However, the unbalanced axial force between stator and rotor may distort the structure, causing vibration, noise, and reduced lifetime.

- **Double-stator / Single-rotor (DSSR)** The rotor is placed between two stators.

- **Single-stator / Double-rotor (SSDR)** Here the stator is placed between two rotors, resulting in a symmetrical structure that balances axial forces. This improves vibration behavior and extends machine lifetime .
- **Multi-stator / Multi-rotor (MSMR)** With N stators and $(N+1)$ rotors, this configuration increases torque and power density without enlarging the motor diameter, making it suitable for high-torque applications such as ship propulsion systems.

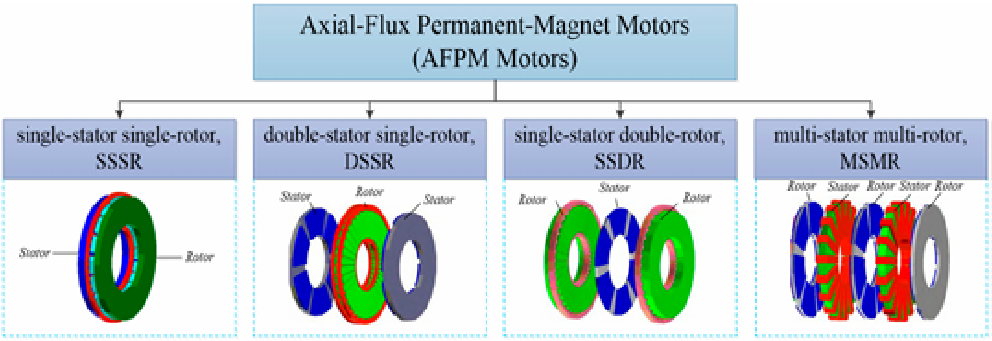

Figure 2.2: Four typical types of topological structures of AFPM motors

It is possible to further subdivide each of these topologies according to the following criteria:

- **Back iron configuration**, i.e., whether the stator and/or rotor include back iron
- **Winding arrangement** (concentrated or distributed windings)
- **Magnet placement**, specifying the location of the permanent magnets within the structure

2.2.1 Single-stator/Single-rotor SSSR

This is the most straightforward AFPM configuration, consisting of one stator and one rotor, as shown in Figure 2.3. Its main features include:

- **Compact structure** with a relatively large aspect ratio.
- **Limited torque capacity** compared to other AFPM topologies.

- **Unbalanced axial forces**: all local axial forces between rotor and stator add up without compensation, unlike in RFPM machines where local radial forces cancel each other.For large-scale machines, these axial forces can reach the order of kilonewtons, potentially causing significant **mechanical issues**.
- To mitigate this, **reinforced bearings** and a **thicker rotor disc** are often required .

In double-sided AFPM machines, by contrast, the axial forces can be compensated more effectively, improving reliability.

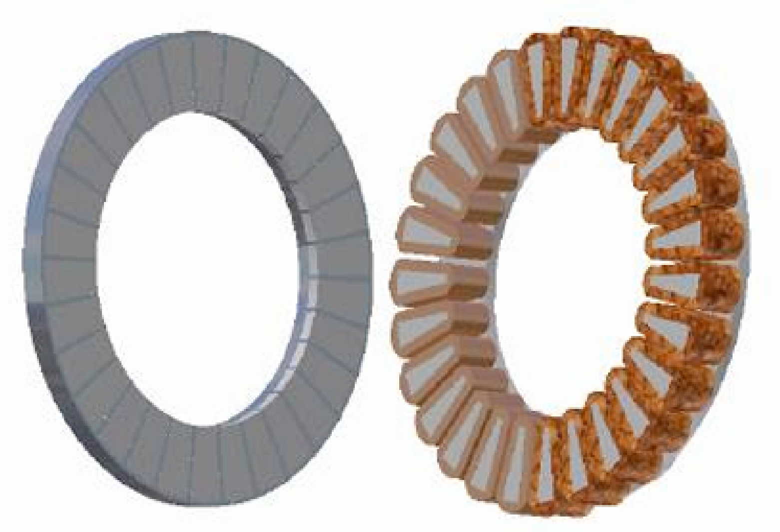

Figure 2.3: Single sided machine

2.2.2 Double-stators/Single-rotor DSSR

This configuration consists of a single rotor, equipped with permanent magnets, placed between two, see Figure 2.4 and Figure 2.7. Its main characteristics include:

- **Magnet arrangement**: - In the **North–North** configuration, the magnetic flux flows circumferentially along the rotor back iron. - In the **North–South** configuration, the flux flows axially through the rotor, making the rotor back iron unnecessary. This reduces axial length, machine weight, and rotor core losses [7].
- **Winding connection**: - If the two stator windings are connected in **parallel**, the current in each stator is halved. - If connected in **series**, the two stators

generate equal and opposite axial forces, which improves mechanical balance and reduces stress on bearings.

- **Air-gap definition**: the total air gap is determined by the sum of the two mechanical clearances and the magnet thickness.
- **Mechanical integration**: since the stators are placed on the outer sides of the machine, integration into the vehicle chassis is facilitated.

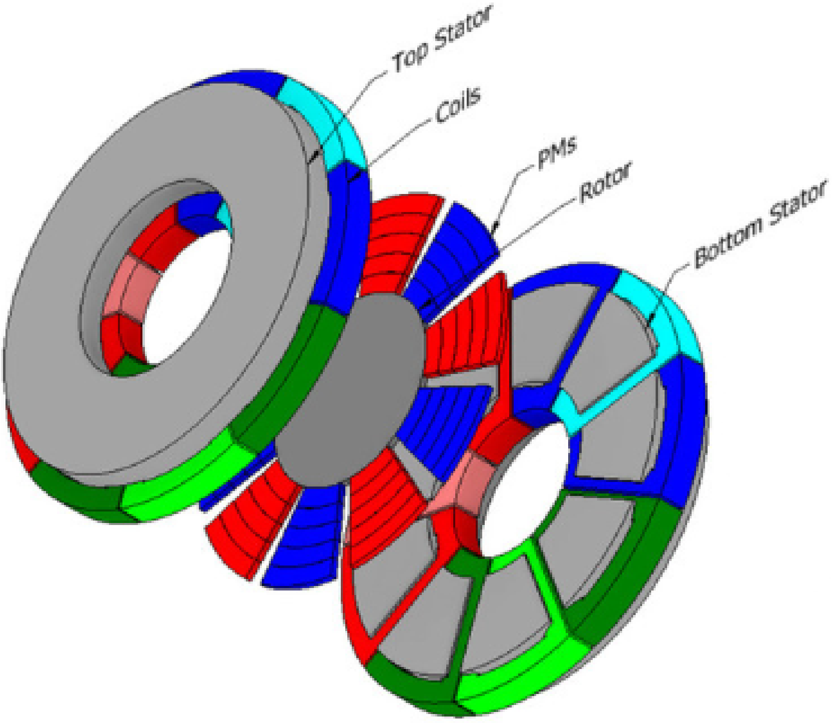

Figure 2.4: Double stator single rotor [8].

2.2.3 Single-stator/Double-rotors SSDR

This configuration places the stator between two rotors, resulting in a symmetrical structure that naturally balances the axial forces, see Figure 2.5 and Figure 2.7. Depending on the stator structure, several configurations of SSDR AFPM machines can be identified in the literature [9, 6]:

- **Slotless stator (TORUS machine):** In this topology, the stator winding is placed directly around the stator core without slots. This configuration eliminates slotting effects and therefore suppresses cogging torque while also reducing harmonic distortion of the air-gap magnetic field. As reported in the literature, slotless AFPM machines can exhibit reduced eddy current and hysteresis losses at high electrical frequency due to the smoother magnetic field distribution in the air gap [9, 10, 6].

However, the effective air gap becomes larger because it includes the mechanical air gap, the insulation surrounding the conductors, and the magnet thickness. Consequently, a larger permanent magnet volume is typically required to maintain the desired air-gap flux density [9, 7].

- **Slotted stator:** In this configuration, the stator includes slots where the windings are placed. The presence of slots reduces the effective air gap compared to the slotless topology, which decreases the required permanent magnet volume and generally allows higher torque density and efficiency [9, 6]. However, the interaction between the rotor magnets and the stator slots introduces cogging torque and torque ripple, which must be mitigated through appropriate design strategies.

- **Coreless stator (YASA machine):** In coreless AFPM machines, the stator winding is supported by a non-magnetic and non-conductive structure or wound around independent stator teeth, as shown in Figure 2.6. This configuration eliminates stator core losses and significantly reduces cogging torque while allowing a compact axial structure [9, 6]. However, the absence of an iron core reduces the magnetic flux concentration capability, which may require increased magnet volume to achieve the desired torque level.

The choice between slotted, slotless, or coreless stator designs also depends on the permanent magnet arrangement and the targeted performance objectives, such as torque density, efficiency, manufacturability, and thermal behavior [9, 6].

(a) Double rotor slotted

(b) Double rotor slottless

Figure 2.5: Double rotor single stator machine [7].

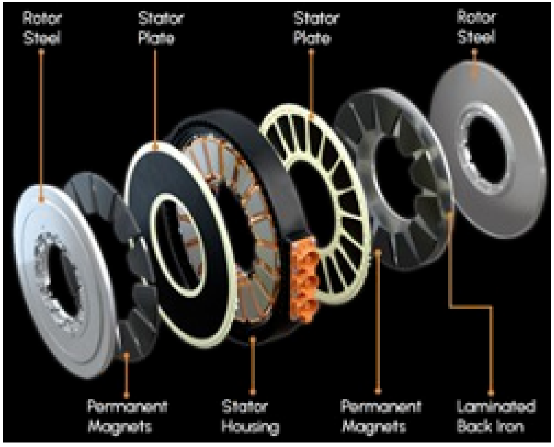

Figure 2.6: YASA motor [7].

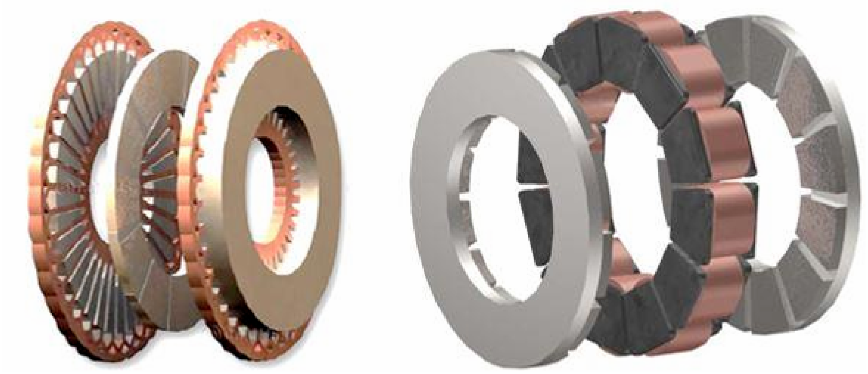

Figure 2.7: Structure with double stator (on the left) and with double rotor

2.2.4 Multi-stator/Multi-rotor MSMR

This configuration consists of multiple modules (stators and rotors) stacked along the shaft axis, Figure 2.8 hows the structure of an MSMR machine. By increasing the number of discs, the torque and maximum power can be enhanced without increasing the diameter of the machine, which is often limited by dimensional constraints.

However, the size of each disc is limited by several factors:

- **Axial forces** acting on the bearings, which increase with the number of stages.
- **Mechanical integrity** of the joints between the rotor and the shaft.
- **Disc stiffness**, which must be sufficient to withstand both electromagnetic and mechanical stresses.
- **Available axial space**, especially critical in automotive and aerospace applications.

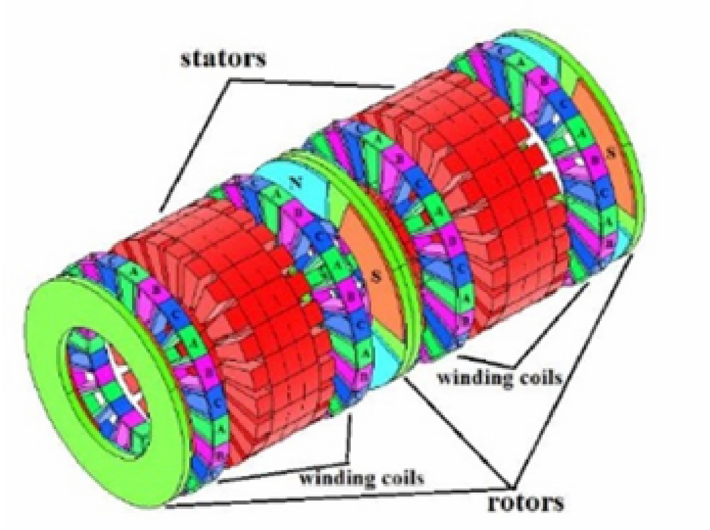

Figure 2.8: Multidisc machine MSMR [7].

2.3 Structural Configuration of AFPM Machines

2.3.1 Influence of Materials on Performance

The performance of AFPM machines strongly depends on the materials adopted for both active and structural components. In the present work, the stator and rotor yokes are modeled using M-19 electrical steel, as selected in the FEMM material library. This non-oriented silicon steel grade offers a good compromise between magnetic performance, mechanical robustness, and cost, making it suitable for medium and high speed electrical machines. Its relatively high magnetic permeability and moderate core losses allow efficient flux guidance within the stator and rotor back-iron while limiting hysteresis and eddy current losses.

Permanent magnets represent the most critical active component, as their remanence and coercivity directly determine the achievable air-gap flux density. In the proposed AFPM design, NdFeB N40 grade magnets are employed. This material provides high remanent flux density and energy product, enabling elevated torque and power density. However, NdFeB magnets exhibit limited thermal stability compared to other rare-earth materials, which motivates careful consideration of operating temperature and cooling strategies.

For the soft magnetic components, alternative materials such as amorphous or nanocrystalline alloys may offer reduced core losses, particularly under high-frequency excitation. Similarly, soft magnetic composites (SMCs) enable three-dimensional flux paths and reduced eddy current losses due to their high electrical resistivity. Despite these advantages, such materials often introduce higher costs and manufacturing complexity.

Overall, the efficiency and power density of AFPM machines result from a trade-off between magnetic performance, thermal behavior, cost, and manufacturability. In this context, the selected combination of M-19 electrical steel for the magnetic cores and N40 NdFeB magnets represents a balanced solution aligned with the performance targets and modeling assumptions of the present study.

2.3.2 Winding Configurations and Design Considerations

The stator winding configuration plays a fundamental role in determining the electromagnetic performance, efficiency, and reliability of electrical machines.

From a topological perspective, stator windings can be broadly classified into:

- **Distributed windings**: coils are distributed over several slots per pole per phase, producing a nearly sinusoidal magnetomotive force (MMF) distribution along the air gap. This configuration typically results in reduced harmonic content. However, distributed windings are characterized by longer end-windings, which increase copper usage and Joule losses.

- **Concentrated windings**: coils are wound around individual teeth. A common implementation is the **fractional-slot concentrated winding (FSCW)**, in which the number of slots per pole per phase is smaller than unity. This configuration offers several practical advantages, including significantly shorter end-windings, reduced copper losses, higher slot fill factor, and simplified manufacturing.

In addition to this classification, both concentrated and distributed windings can be further divided into:

- **Single-layer windings**: coils are wound on alternate teeth, resulting in low mutual inductance between adjacent phases and improved thermal and magnetic isolation. This structure is particularly attractive for fault-tolerant applications and high-speed operation due to its relatively high self-inductance.
- **Double-layer windings**: each tooth accommodates two coil sides belonging to different phases. This arrangement generally provides a higher fundamental winding factor and improved torque production capability, while also contributing to a reduction in torque ripple.

As a consequence, double-layer windings are often preferred when smoother torque and enhanced electromagnetic performance are required.

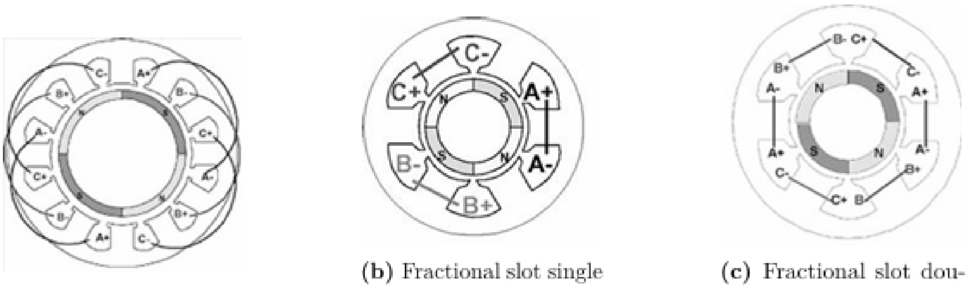

(a) Distributed winding

(b) Fractional slot single layer winding

(c) Fractional slot double layer winding

Figure 2.9: Winding types [11].

Chapter 3

Sizing Procedure

In this chapter, an **electromagnetic sizing methodology** is proposed for the preliminary design of AFPM machines. This procedure is based on the analytical approach presented in [1, 12], which provides the reference framework for the formulation and design steps.

A sizing procedure is proposed to define a consistent machine geometry. The resulting design is subsequently evaluated using a 2D analytical model, which serves to validate the proposed dimensioning approach.

The procedure is entirely analytical and follows an iterative process, where the machine diameters are gradually increased until the imposed design constraints are satisfied and the target performance is reached.

The sizing procedure is applied to the dimensioning of a single-stage AFPM machine. Once the geometry of the elementary stage is defined, it can be replicated or mirrored to obtain different AFPM configurations. In this way, multi-stage machines such as double-stator or double-rotor topologies can be derived from the geometry of a single stage.

3.1 User Inputs and Sizing Procedure

In order to establish a reliable preliminary design framework for AFPM machines, a structured methodology is required. While the fundamental design principles stem from classical electromagnetic theory—such as Maxwell's equations, flux continuity, and Ampère's law—their translation into practical sizing requires a careful definition of input parameters and design constraints. This section introduces the essential inputs that guide the sizing algorithm and describes the rationale behind each category of parameters, from performance requirements to material specifications and geometrical constraints. The overall workflow of the proposed sizing approach is illustrated in Fig. 3.1. The process begins with the collection of user-defined input values, followed by initial calculations and progressive lamination sizing. Equivalent circuit parameters are then derived, and the procedure iterates until all design requirements are satisfied. The logic is not only computationally efficient but also offers the designer a deeper physical insight into how each parameter affects machine performance.

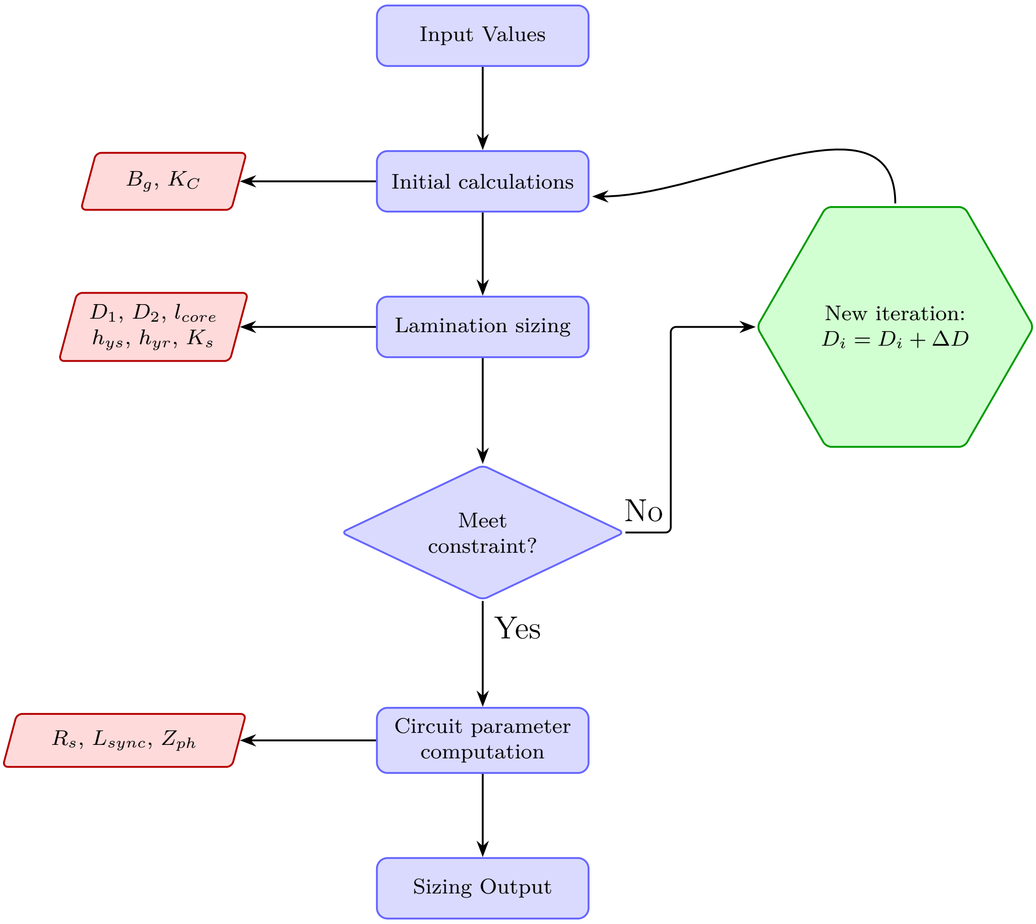

Figure 3.1: Flowchart of the sizing procedure for AFPM machines.

3.1.1 Input Parameters

The required design input data encompass four categories: (i) target performances, (ii) material specifications, (iii) stress loading indexes, and (iv) geometric and winding specifications. These inputs are summarized in Table 3.1. Each parameter has a clear physical interpretation and a direct impact on electromagnetic behavior: for instance, torque is linked to the interaction between the stator current loading and the rotor flux, while speed determines the electrical frequency and thus influences the calculation of inductive parameters.

Parameter	**Symbol**	**Unit**
Target Performance		
Torque	T_r	Nm
Speed	n_r	rpm
Phase voltage	V_r	V
Material Specifications		
Lamination stack coefficient	k_{fe}	–
PM remanence	B_r	T
PM relative permeability	μ_r	–
Stress Loading Indexes		
Max. teeth flux density	B_{ts}	T
Max. stator yoke flux density	B_{ys}	T
Max. rotor yoke flux density	B_{yr}	T
Max. linear current density	$K_{s,\max}$	A/cm
Slot current density	J_{rms}	A/mm^2
Geometric and Winding Specifications		
Aspect ratio	λ_{AFM}	–
Pole pairs	p	–
Slots	N_s	–
Shaft diameter	D_{sh}	mm
Airgap thickness	h_{gap}	mm
Magnet axial thickness	h_{pm}	mm
Magnet pole arc ratio	α_{pm}	–
Slot enclosure dims.	w_{so}, h_{ls}, h_{es}	mm
Copper fill factor	k_{cu}	–
PM radial length	l_{PM}	mm
Winding pitch reduction	n_{sr}	–

Table 3.1: Design Input Values

The selection of these inputs is inherently a trade-off: for example, a higher current density can improve torque density but aggravates thermal stress, while a thinner airgap enhances flux linkage but increases sensitivity to mechanical tolerances. Literature provides recommended ranges for several of these values depending on machine type and cooling configuration [13, 14].

3.1.2 Design Assumptions

The proposed sizing procedure relies on the following assumptions, which balance analytical tractability with physical accuracy:

- Constant permeability of magnetic materials (no saturation considered in preliminary stage).
- Semi-open, squared-shaped slots.

These simplifications make the method particularly suited as a first-step analytical tool, allowing designers to obtain an initial geometry that can later be refined using numerical simulations or optimization algorithms.

3.2 Preliminary Calculations

Before lamination sizing, several preliminary quantities must be evaluated. Figure 3.2 shows the main axial and radial dimensions of the AFPM machine. These parameters establish the geometrical framework for electromagnetic analysis.

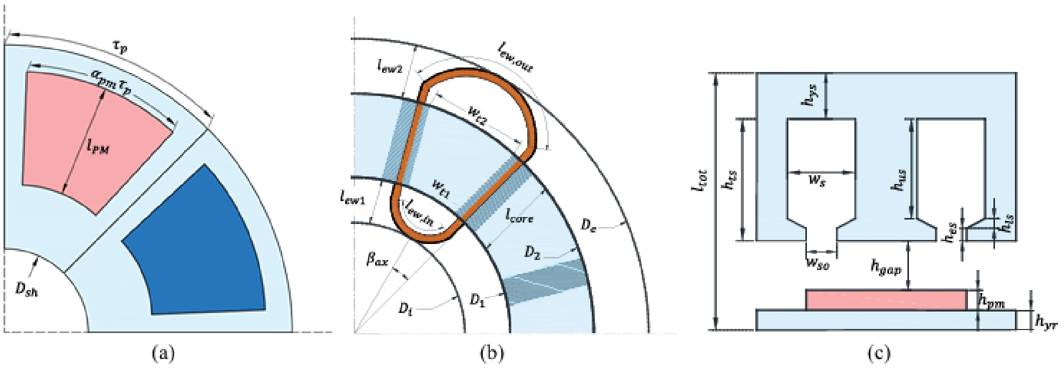

Figure 3.2: Main AF motor dimensions: (a) rotor strcture, (b) stator and winding coils, (c) axial view with core, slot, and magnet dimension [1].

We begin the analysis of the sizing procedure by considering the aspect ratio of the machine, as it represents a fundamental geometrical parameter that strongly influences the electromagnetic performance.

The aspect ratio λ_{AFM} is defined as the ratio between the inner and outer diameter of the lamination. It influences the machine geometry, making it more "disc-shaped" or "ring-shaped," and directly affects the torque production capability. Mathematically, it can be expressed as:

$$\lambda_{AFM} = \frac{D_1}{D_2}, \tag{3.1}$$

where D_1 is the inner diameter and D_2 the outer diameter of the lamination.

In the following analysis, we assume as a reference the value

$$\lambda_{AFM} = \frac{1}{\sqrt{3}}, \tag{3.2}$$

which is reported in literature as a suitable choice to maximize the electromagnetic torque production [15].

It is important to remark, however, that in practical design scenarios the choice of λ_{AFM} is also constrained by the available radial space and mechanical integration requirements. Therefore, while the value $1/\sqrt{3}$ provides a useful theoretical benchmark, different applications may require the adoption of alternative ratios to comply with packaging constraints or to optimize the trade-off between torque density, efficiency, and manufacturability.

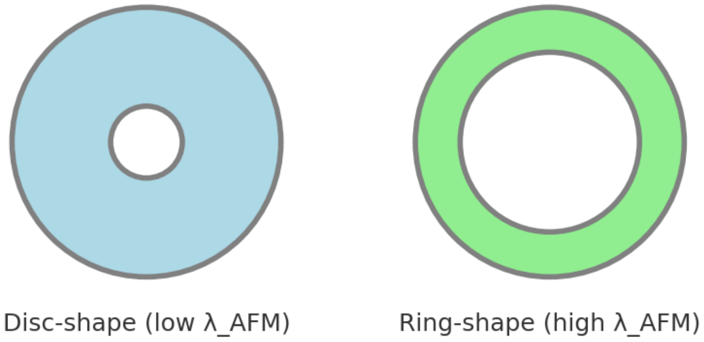

Figure 3.3: Effect of the aspect ratio λ_{AFM} on the machine geometry.

As shown in Fig. 3.3, a low value leads to a more disc-like structure, while a high value results in a ring-shaped configuration.

The electromagnetic torque originates from the interaction between the peak of the fundamental component of the airgap flux density and the current distribution across the stator slots, in accordance with the fundamental law of electromagnetic energy conversion. In this simplified analytical approach, the flux density distribution produced by the permanent magnets (PMs) is assumed to be square-shaped and radially uniform, as illustrated in Fig. 3.4. Under this assumption, the peak airgap flux density B_g can be expressed as:

$$B_g = B_r \cdot \frac{h'_{pm}}{h'_{pm} + h'_{gap}}, \tag{3.3}$$

where $h'_{pm} = \dfrac{h_{pm}}{\mu_{pm}}$ is the equivalent magnet height, obtained by considering h_{pm} as the axial thickness of the permanent magnet and μ_{pm} as its relative magnetic permeability.

The equivalent airgap thickness h'_{gap}, corrected with Carter's coefficient K_C [13], is then defined as:

$$h'_{gap} = K_C \cdot h_{gap}. \tag{3.4}$$

Finally, the fundamental component of the square flux density distribution is given by:

$$B_{g1} = \frac{4}{\pi} B_g \cdot \sin\left(\frac{\pi}{2} \cdot \alpha_{pm}\right). \tag{3.5}$$

Equation (4.5) above provides, denoted as B_{g1}, is particularly relevant since it directly determines the electromagnetic torque production as well as the induced back-EMF waveform in the machine.

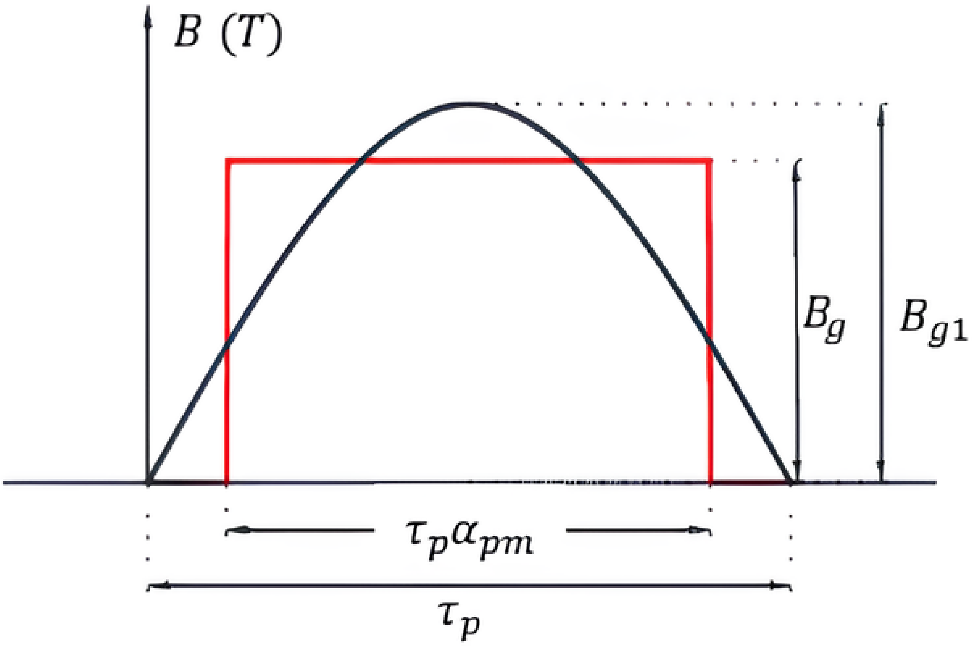

Figure 3.4: Idealized square flux density distribution across the airgap [1].

These preliminary steps ensure that the algorithm begins from a physically consistent flux distribution, bridging material properties with geometric selections.

3.3 Magnetic Core Sizing

The lamination sizing procedure relies on iterative adjustment of the inner diameter until electromagnetic loading constraints are met. Starting with the shaft diameter as the minimum value, successive iterations increase the inner lamination diameter D_1 until the stopping criteria are satisfied.

3.3.1 Step 1: Geometry initialization and diameters

The lamination sizing procedure is performed iteratively by increasing the inner lamination diameter D_1 until the imposed electromagnetic loading constraints are met. The first iteration starts from the shaft diameter D_{sh} (used as initialization for the mechanical inner diameter D_i). The relationship between the mechanical inner diameter D_i and the lamination inner diameter D_1 depends on the winding layout through the angular parameter β_{ax}, defined as

$$\beta_{ax} = \begin{cases} \dfrac{\pi}{2p}, & \text{for DW,} \\ \dfrac{\pi}{N_s}, & \text{for FSCW.} \end{cases} \tag{3.6}$$

Given β_{ax}, D_1 is obtained from D_i via a purely geometric relation. Two cases are considered:

$$D_1 = \begin{cases} \dfrac{D_i}{\dfrac{1}{\cos\beta_{ax}} - \tan\beta_{ax}}, & p < 6, \\ \dfrac{D_i}{\cos\beta_{ax} - \sin\beta_{ax}}, & p \geq 6. \end{cases} \tag{3.7}$$

Once D_1 is known, the stator lamination outer diameter is imposed by the chosen aspect ratio:

$$D_2 = \frac{D_1}{\lambda_{AFM}}. \tag{3.8}$$

Two auxiliary geometric quantities are then defined and used throughout the sizing:

$$D_e = D_2\left(\sin\beta_{ax} + \cos\beta_{ax}\right), \tag{3.9}$$

$$l_{core} = \frac{D_2 - D_1}{2}. \tag{3.10}$$

Because the air-gap flux of AFPM machines is not uniform along the radius, the flux per pole ϕ_{pole} is evaluated over the average stator diameter $D_m = (D_1 + D_2)/2$ and the PM radial length l_{PM} which can be approximated as the l_{core}, yielding:

$$\phi_{pole} = \frac{\pi\, D_m\, \alpha_{pm}\, l_{PM}}{2p} \cdot B_g, \tag{3.11}$$

where α_{pm} is the magnet pole-arc ratio and B_g is the average air-gap flux density previously defined.

Design note. Equations (3.6)–(3.11) set the purely geometric scaffold of the axial-flux machine. In practice, D_1 grows iteratively (with D_2 following from (3.8)) until the electromagnetic and thermal constraints are satisfied in the subsequent steps (yoke sizing, slot/tooth sizing, current loading, and stopping criterion).

3.3.2 Step 2: Yoke and tooth sizing

Once the inner and outer lamination diameters are known, the magnetic core is sized to keep the flux densities below the prescribed limits for teeth and yokes. Because the radial flux is higher at the outer diameter, yoke heights are computed at D_2 to satisfy the stress indexes.

Yoke heights. Assuming negligible inter–pole leakage in this preliminary step, the stator and (laminated) rotor yoke heights follow:

$$h_{ys} = \frac{\pi\, D_2\, \alpha_{pm}\, B_g/(2p)}{2\, B_{ys}\, k_{fe}}, \qquad h_{yr} = \frac{\pi\, D_2\, \alpha_{pm}\, B_g/(2p)}{2\, B_{yr}\, k_{fe}}, \tag{3.12}$$

where α_{pm} is the pole-arc ratio, B_g the average air-gap flux density, B_{ys} and B_{yr} the admissible yoke flux densities for stator and rotor, and k_{fe} the lamination stacking factor.

Tooth and slot widths. Teeth are most stressed at the inner diameter D_1. Imposing the tooth flux density limit B_{ts} leads to the inner-tooth width:

$$w_{t1} = \frac{B_g\, \pi\, D_1/N_s}{B_{ts}\, k_{fe}} \tag{3.13}$$

with N_s the number of stator slots. Under the squared-slot assumption adopted in this sizing, the slot opening (slot width) and the tooth width at the outer diameter are:

$$w_s = \frac{\pi\, D_1}{N_s} - w_{t1}, \tag{3.14}$$

$$w_{t2} = \frac{\pi\, D_2}{N_s} - w_s \tag{3.15}$$

3.3.3 Step 3: Torque, useful slot area, and linear current density

Once the tooth and yoke dimensions satisfy the admissible flux densities, the electromagnetic performance can be related to the copper allocation and current loading.

Electromagnetic torque. Under the square-wave PM flux assumption, the average electromagnetic torque can be written as

$$T_{em} = \frac{\sqrt{2}}{16}\, k_{w1}\, A_{cu}\, (D_2^2 - D_1^2)\, N_s\, B_{g1}\, J_{rms}, \tag{3.16}$$

where k_{w1} is the fundamental winding factor, A_{cu} is the total copper area per slot effectively carrying current, N_s is the number of stator slots, B_{g1} is the fundamental component of the air-gap flux density, and J_{rms} is the rms slot current density. *Remark.* For double-stage AF machines, the expected torque is approximately doubled with the same per-stage quantities.

Useful slot area and useful height. Given a prescribed copper fill factor k_{cu}, the useful slot area A_{us} follows from the copper area:

$$A_{us} = \frac{A_{cu}}{k_{cu}}. \tag{3.17}$$

With the squared-slot assumption, the corresponding useful slot height is

$$h_{us} = \frac{A_{us}}{w_s}, \tag{3.18}$$

where w_s is the slot width obtained in Step 2.

Linear current density. The linear current density is evaluated at the inner diameter D_1 as

$$K_s = k_{w1}\, J_{rms} \left(\frac{N_s\, A_{cu}}{\pi\, D_1} \right). \tag{3.19}$$

Equation (3.19) links the copper allocation (A_{cu}) to the effective current loading on the inner circumference and will be used in the stopping criterion of Step 4.

Design note. Equations (3.16)–(3.19) show the classical trade-off: increasing A_{cu} and/or J_{rms} boosts T_{em} and K_s, but raises thermal stress and may constrain k_{cu} (manufacturability). In practice, A_{cu}, J_{rms}, k_{cu}, and cooling strategy must be co-designed so that the thermal index in Step 4 is respected while meeting target torque.

3.3.4 Step 4: Stopping criterion

The stopping condition is formulated in terms of the maximum admissible thermal loading given by the product of the linear current density K_s and the rms current density J_{rms}:

$$K_s \cdot J_{rms} \leq (K_s \cdot J)_{\max}. \tag{3.20}$$

The product $K_s J_{rms}$ is directly related to the Joule losses generated in the stator windings and therefore to the thermal loading of the machine. Since the temperature rise of the stator slots is proportional to the Joule losses, limiting this product allows the designer to control the winding over temperature.

Moreover, very high values of $K_s J_{rms}$ typically occur when the available circumferential space is limited. In such cases, the stator design routine tends to converge towards slot geometries that are excessively deep and narrow in order to accommodate the required current loading. These tapered slot shapes are generally undesirable from both thermal and manufacturing perspectives.

For this reason, the iterative design procedure terminates when the value of $K_s J_{rms}$ falls below the admissible constraint imposed by the designer, ensuring a thermally feasible and geometrically consistent stator design.

3.4 Circuit Parameters Calculation

Once the lamination sizing process is completed, the equivalent circuit parameters of the machine can be determined. This step provides the link between the purely geometrical–electromagnetic sizing of the previous chapter and the electrical behavior of the AFPM motor. The goal is to obtain the quantities needed for performance prediction: phase resistance, synchronous inductance, no-load back-EMF, and the number of conductors in series per phase.

The per-phase equivalent circuit of a surface-mounted AFPM synchronous motor is shown in Fig. 3.5, together with the corresponding phasor diagram. Here, $\overline{V}_r$ is the rated phase voltage, R_s the phase resistance, L_{sync} the synchronous inductance, $\overline{E}_0$ the no-load back-EMF phasor proportional to rotor speed and flux linkage, and $\overline{I}_s$ the rated current phasor. Assuming that the current is entirely aligned with the q-axis, the voltage equation is expressed as:

$$\overline{V}_r = \overline{E}_0 + R_s \, \overline{I}_s + j \, \omega_e L_{sync} \, \overline{I}_s, \tag{3.21}$$

where ω_e is the electrical angular frequency.

Design note. This formulation highlights the balance between the induced EMF and the voltage drops on resistance and inductance. It provides the analytical

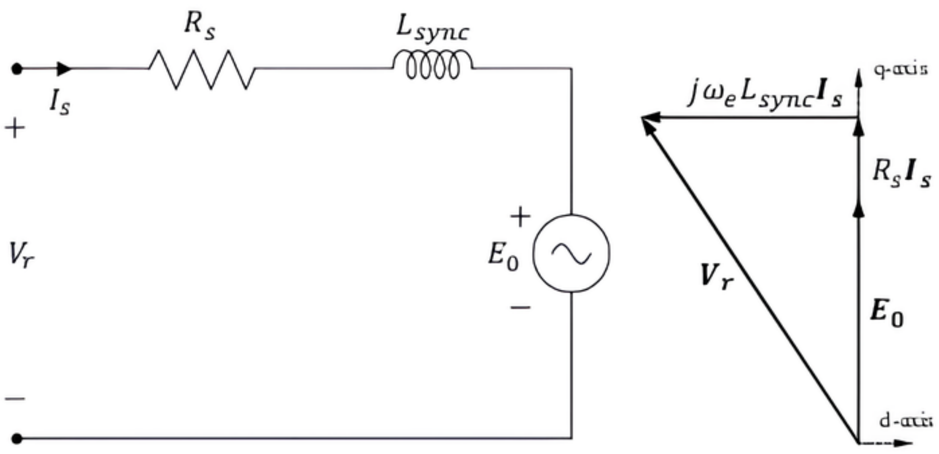

Figure 3.5: Equivalent circuit of a non-salient PM synchronous AF motor and its phasor diagram [1].

foundation for calculating Z_{ph} (the turns in series per phase) and will be further detailed in the next steps

3.4.1 Phase resistance

The first parameter of the equivalent circuit is the phase resistance R_s, which accounts for copper losses in the stator winding. For a winding with Z_{ph} conductors connected in series per phase, R_s can be expressed as:

$$R_s = \rho_{cu} \cdot \frac{Z_{ph}^2 \cdot l_{turn,ave}}{4 \cdot q \cdot p \cdot A_{cu}}, \tag{3.22}$$

where ρ_{cu} is the electrical resistivity of copper at the operating temperature, q is the number of slots per pole per phase, p is the pole pair number, and A_{cu} is the cross-sectional copper area per conductor.

The average turn length $l_{turn,ave}$ depends on the winding arrangement and can be estimated as:

$$l_{turn,ave} = 2\,(l_{slot} + l_{ew,ave}), \tag{3.23}$$

where l_{slot} is the slot length and $l_{ew,ave}$ the average end-winding length. The latter can be approximated differently depending on the winding type:

$$l_{ew,ave} = \begin{cases} \left(1 - \dfrac{n_{sr}}{3q}\right) \cdot \dfrac{\pi\,(D_1 + D_2)}{4p}, & \text{for DW,} \\ \dfrac{\pi w_s}{2} + \dfrac{\pi\,(w_{t1} + w_{t2})}{4}, & \text{for FSCW.} \end{cases} \tag{3.24}$$

Design note. The phase resistance strongly influences both copper losses and the voltage drop across the winding. Minimizing R_s improves efficiency, but requires careful trade-offs: longer end-windings or higher slot fill factors reduce compactness and can increase thermal stress. Accurate estimation of $l_{turn,ave}$ is therefore essential, especially in AFPM machines where end-windings significantly contribute to copper losses.

3.4.2 Inductance calculation

The synchronous inductance L_{sync} of an AFPM machine cannot be described by a single simple expression, since it includes contributions from different flux paths. A practical analytical estimation is obtained by decomposing L_{sync} into the sum of magnetizing and leakage components:

$$L_{sync} = L_m + L_{gap} + L_{slot} + L_{end} + L_{tt}, \tag{3.25}$$

where:

- L_m: magnetizing inductance (main flux),
- L_{gap}: air-gap leakage inductance,
- L_{slot}: slot leakage inductance,
- L_{end}: end-winding leakage inductance,
- L_{tt}: tooth-tip leakage inductance.

Magnetizing inductance. For DW and FSCW, different formulations are adopted:

$$L_m = \begin{cases} \dfrac{3}{2}\left(\dfrac{Z_{ph}\,k_{w1}}{\pi p}\right)^2 \mu_0 \pi D_{ag} l_{core} \dfrac{1}{h'_{gap}}, & \text{for DW,} \\ L_m = \frac{4}{\pi}\cdot\frac{l_{core}\,\mu_0}{h'_{gap}}\cdot\frac{q}{N_s}\cdot(3k_{ws}Z_{ph})^2\cdot D_{ag}., & \text{for FSCW,} \end{cases} \tag{3.26}$$

where $D_{ag} = (D_1 + D_2)/2$ is the average air-gap diameter and h'_{gap} is the Carter-corrected air-gap length.

Air-gap leakage. The harmonic air-gap leakage factor σ_{gap} has minor impact for integral-slot DW but is more relevant for FSCW:

$$L_{gap} = \sigma_{gap}\,L_m. \tag{3.27}$$

Slot leakage. Slot leakage flux paths contribute significantly to L_{sync}, and are expressed differently for DW and FSCW:

$$L_{slot} = \begin{cases} \dfrac{\mu_0 Z_{ph}^2 l_{core}}{8pq} \left(\lambda_1 + \lambda_2 + \left(2 - \dfrac{n_{sr}}{q}\right) \lambda_{12}\right), & \text{for DW,} \\ \dfrac{12}{N_s}\, \mu_0 Z_{ph}^2 l_{core}\, \lambda_{slot}, & \text{for FSCW.} \end{cases} \tag{3.28}$$

End-winding inductance. The contribution of the end-winding depends strongly on the winding type and surrounding environment:

$$L_{end} = \begin{cases} 0.44\, \mu_0\, p\, q^2\, Z_{ph}^2\, l_{ew,ave}, & \text{for DW,} \\ \mu_0\, \mu_{env} \dfrac{12 h_{us}}{\pi N_s} \left(\dfrac{Z_{ph}\, l_{ew,ave}}{4pq}\right)^2, & \text{for FSCW,} \end{cases} \tag{3.29}$$

where μ_{env} is the relative permeability of the end-winding environment (typically 1.2–2).

Tooth-tip leakage. Finally, the semi-open slot shape is modeled by the tooth-tip leakage:

$$L_{tt} = \frac{12}{N_s}\, \mu_0 Z_{ph}^2\, l_{core}\, k_1 \lambda_{tt}, \tag{3.30}$$

with λ_{tt} the tooth-tip leakage permeance factor and k_1 a correction for slot-sharing phases.

Design note. The inductance calculation is inherently approximate, since leakage paths are three-dimensional and depend on geometry and material nonlinearities. Nevertheless, analytical estimation is essential at this stage: it provides values consistent enough for performance prediction and reduces the number of costly 2D FEM simulations required later in the design cycle.

3.4.3 Conductors in series per phase

The final step of the circuit parameter calculation is the determination of the number of conductors in series per phase Z_{ph}. This parameter ensures consistency between the imposed rated voltage and the analytical circuit model.

No-load back-EMF. The no-load EMF can be expressed as:

$$E_0 = 4.44\, f_r\, k_{ws}\, \phi_{pole1} \frac{Z_{ph}}{2}, \tag{3.31}$$

where f_r is the rated frequency, k_{ws} the winding factor, and ϕ_{pole1} the fundamental component of the flux per pole.

Armature current. The rated armature current per phase is linked to slot current density as:

$$I_s = (J_{rms}\, A_{cu}) \cdot \frac{N_s}{3\, Z_{ph}}, \tag{3.32}$$

where A_{cu} is the effective copper area per slot and N_s the number of slots.

Dependence on Z_{ph}. Both resistance and inductance depend on Z_{ph}, while E_0 is linear and I_s is inversely proportional:

$$R_s = K_R \cdot (Z_{ph})^2\,, \qquad L_{sync} = K_L \cdot (Z_{ph})^2\,, \tag{3.33}$$

$$E_0 = K_E \cdot Z_{ph}, \qquad I_s = \frac{K_I}{Z_{ph}}, \tag{3.34}$$

where K_R, K_L, K_E, and K_I are constants that can be obtained rearranging the previous formulations.

Final relation. Substituting these relations into the phasor voltage equation yields:

$$\overline{V}_r = \overline{E}_0 + R_s\, \overline{I}_s + j\, \omega_e L_{sync}\, \overline{I}_s. \tag{3.35}$$

From which the required number of turns in series per phase is obtained:

$$Z_{ph} = \frac{V_r}{\sqrt{(K_E + K_R K_I)^2 + (\omega_e K_L K_I)^2}}. \tag{3.36}$$

Design note. The calculation of Z_{ph} closes the analytical loop of the sizing procedure: it guarantees that the rated phase voltage is consistent with the predicted EMF and voltage drops. Because Z_{ph} also determines copper length and resistance, its proper selection is fundamental to ensure both performance and efficiency.

Implementation note. All the analytical calculations presented in this chapter, including the evaluation of phase resistance, inductances, and the determination of the number of conductors in series per phase, were implemented and verified using MATLAB scripts.

For clarity, the MATLAB scripts implementing this analytical procedure are reported in Appendix A.

3.5 Case Study

The AFPM machine considered in this study corresponds to a **single-stage configuration**, consisting of a **single stator and a single rotor** (1S1R topology) separated by a single active air-gap (`tplg = "Single"`). The rotor is equipped with **surface-mounted permanent magnets** (SPM), a configuration commonly adopted in axial-flux machines due to its structural simplicity and favourable electromagnetic characteristics.

The stator is designed with a three-phase **fractional-slot concentrated winding** (FSCW) arranged in a **double-layer configuration** (`wdtype = "Conc"`, `wdLayers = "DL"`) and connected in star.

The adopted slot–pole combination is

$$N_s = 12, \qquad 2p = 10 \text{ (10 poles, corresponding to } p = 5 \text{ pole pairs)}, \qquad m = 3.$$

This choice satisfies the winding feasibility condition

$$q = \frac{N_s}{2pm},$$

and enables the implementation of a compact concentrated winding with reduced end-winding length.

In this thesis, a fractional-slot double-layer concentrated winding configuration (case c in Figure 2.9) has been adopted. This solution provides a higher fundamental winding factor and reduced torque ripple compared to the single-layer arrangement, while preserving the compact end-winding structure typical of concentrated windings.

3.5.1 Design Targets and Rated Operating Point

The sizing and modelling activities are referred to the following rated operating point:

- Rated torque: $T_r = 40$ N m
- Rated speed: $n_r = 600$ rpm
- Rated phase voltage: $V_{ph} = 145$ V
- DC-link voltage: $V_{dc} = 366.16$ V

The corresponding rated electrical frequency is

$$f_r = \frac{p\, n_r}{60} = \frac{5 \cdot 600}{60} = 50 \text{ Hz}.$$

3.5.2 Sizing Input Parameters

The analytical sizing procedure described in Chapter 3 requires a set of input parameters defining the target performance, material properties, electromagnetic loading limits, and geometric constraints.

The rated torque, speed, and phase voltage determine the electromagnetic loading required from the machine. Material parameters such as the permanent magnet remanence and lamination stacking factor influence the achievable magnetic flux density levels, while the admissible flux density limits in the stator teeth and yokes are selected to avoid excessive magnetic saturation.

The slot current density is chosen according to typical thermal limits for naturally cooled electrical machines. The remaining geometric parameters (slot number, pole number, air-gap length, and magnet dimensions) are defined to ensure a feasible winding layout and a compact machine structure.

The complete set of design input parameters used for the sizing procedure is reported in Table 3.2.

3.5.3 Sizing Results

By applying the analytical sizing procedure described in Chapter 3, the main geometric dimensions and electromagnetic parameters of the AFPM machine are obtained.

These quantities define the machine geometry and the electrical parameters used for the subsequent finite-element modelling in FEMM. The resulting design parameters are summarized in Table 3.3.

Parameter	**Value**	**Unit**
Target Performance		
Torque (T_r)	40	Nm
Speed (n_r)	600	rpm
Phase voltage (V_{ph})	145	V
Material Specifications		
Lamination stack coefficient (k_{fe})	0.958	–
PM remanence (B_r)	1.08	T
PM relative permeability (μ_r)	1.058	–
Permeability of free space (μ_0)	$4\pi \cdot 10^{-7}$	H/m
Stress Loading Indexes		
Max. teeth flux density (B_{ts})	1.8	T
Max. stator yoke flux density (B_{ys})	1.4	T
Max. rotor yoke flux density (B_{yr})	1.4	T
Max. linear current density ($K_{s,\max}$)	($K_{s,\max}$)	A/cm
Slot current density (J_{rms})	7.42	A/mm^2
Geometric and Winding Specifications		
Aspect ratio (λ_{AFM})	0.5775	–
Pole pairs (pp)	5	–
Number of poles (p)	10	–
Slots (N_s)	12	–
Shaft diameter (D_{sh})	50	mm
Airgap thickness (h_{gap})	1	mm
Magnet axial thickness (h_{pm})	5	mm
Magnet pole arc ratio (α_{pm})	0.75	–
Slot enclosure dims. (w_{so})	5	mm
Slot enclosure dims. (h_{ls})	1	mm
Slot enclosure dims. (h_{es})	1	mm
Copper fill factor (k_{cu})	0.307	–

Table 3.2: Design Input Values

Parameter	**Value**	**Unit**
Geometry		
Stator inner diameter (D_1)	126.4	mm
Stator outer diameter (D_2)	218.9	mm
Core axial length (l_{core})	46.2	mm
Yokes		
Stator yoke thickness (h_{ys})	16.96	mm
Rotor yoke thickness (h_{yr})	16.96	mm
Conductors		
Slot area (A_{us})	535.38	mm^2
Copper area (A_{cu})	164.36	mm^2
Slots		
Tooth width (inner) (w_{t1})	16.93	mm
Slot width (w_s)	16.16	mm
Tooth width (outer) (w_{t2})	41.14	mm
Slot height (h_{us})	33.13	mm
Flux Density		
Air gap flux density (B_g)	0.882	T
Fundamental air gap flux density (B_{g1})	1.038	T
Loads		
Current loading (K_s)	34382	A/m
Electromagnetic torque (T_{em})	40.0	N·m
Circuit		
Series turns per phase (Z_{ph})	246	–
Phase resistance (R_s)	0.224	Ω
Synchronous inductance (L_{sync})	0.02155	H
Back-EMF (E_0)	49.7	V
Phase current (I_s)	19.8	A

Table 3.3: Key parameters used for the FEMM model generation computed with the sizing code.

Chapter 4

2D and Q-3D approaches

This chapter investigates simplified modelling strategies for AFPM machines, with particular emphasis on quasi-3D approaches. The objective is to reduce the computational cost of 3D FEA while retaining sufficient accuracy to evaluate key performance indicators such as back-EMF, torque, and flux distribution. These modelling strategies are adopted to validate the analytical sizing procedure and are compared against a high-fidelity 3D reference model developed in [16].

The chapter is structured as follows: first, the general concept of quasi-3D modelling is introduced. Then, different 2D finite element approaches are presented and their reduction procedure from the original 3D problem is illustrated. Subsequently, computational efficiency and accuracy are compared among the methods, and the chapter concludes with a discussion and final remarks.

4.1 2D Finite Element Modelling Approaches

Although AFPM machines are inherently three-dimensional, several authors have proposed strategies to approximate their behaviour using **two-dimensional finite-element models**.

In particular, the methodology presented in [2] introduces alternative 2D modelling approaches that significantly reduce the computational cost of full 3D simulations while maintaining acceptable accuracy in the prediction of the main electromagnetic quantities.

4.1.1 Reduction from 3D to 2D models

The simplified modelling strategies considered in this work are based on a reduction procedure that converts the original three-dimensional AFPM problem into a set of equivalent two-dimensional finite-element models.

This reduction exploits the geometrical symmetry of the machine and consists of slicing the 3D geometry along several radial planes. Each slice represents a radial section of the machine that can be analysed independently using a 2D finite-element model.

The electromagnetic quantities obtained from the different sections are then **combined** to reconstruct the overall behaviour of the original AFPM machine.

This concept is illustrated in Fig. 4.1, which shows the decomposition of a double-rotor AFPM machine into multiple equivalent 2D models.

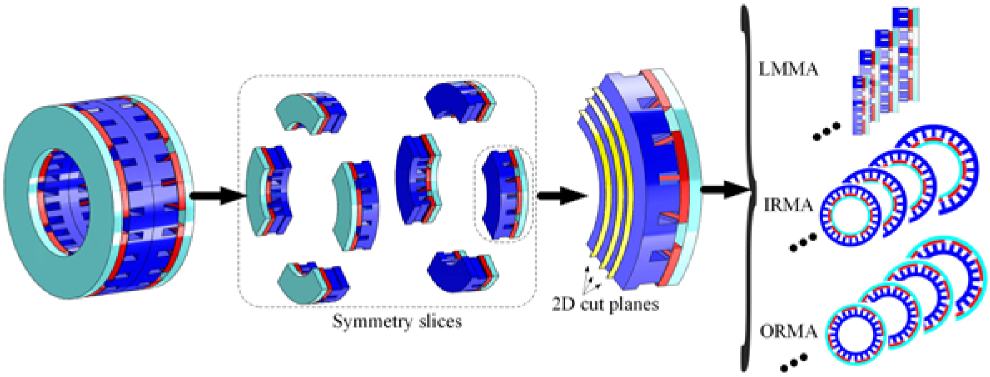

Figure 4.1: Conversion of a 3D AFPM motor into several 2D motor models through symmetry reduction and slicing [2].

The accuracy of the 2D approximation depends on the **number of slices** used in the reduction process. Increasing the number of cut-planes improves the representation of the radial variation of the magnetic field and reduces the error in quantities such as back-EMF, cogging torque, and average torque. However, it also increases the total computational cost.

Therefore, an appropriate compromise between accuracy and computational efficiency must be identified for each machine configuration.

Figure 4.2 compares the flux density distributions obtained using a full 3D finite-element model and different quasi-3D approaches (LMMA, IRMA, and ORMA). The simplified models are able to reproduce the main flux patterns of the 3D solution, although small discrepancies may arise due to the approximations introduced by the 2D representation.

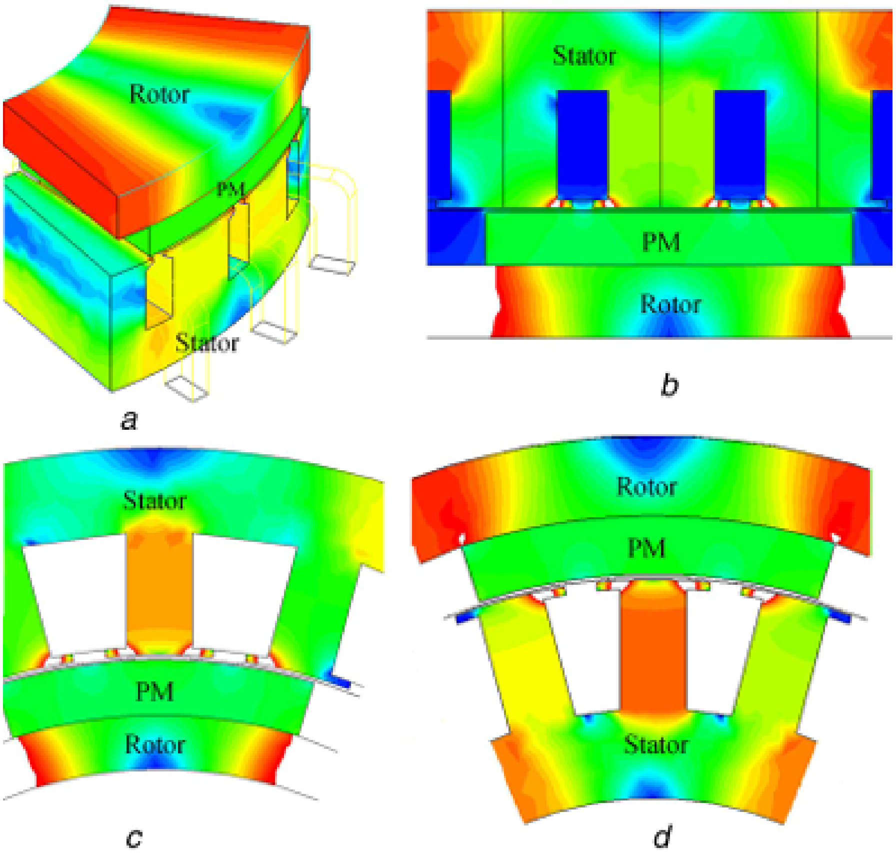

Figure 4.2: Flux density profiles obtained with different modelling approaches: (a) 3D FEA, (b) 2D LMMA, (c) 2D IRMA, (d) 2D ORMA [2].

4.1.2 Equivalent 2D modelling approaches

Following the reduction procedure described above, the AFPM machine can be represented through a set of equivalent 2D models derived from the radial sections.

These simplified representations can be classified into three main categories:

- **Linear Motor Modelling Approach (LMMA)** – the machine is unfolded into equivalent planar models defined at different radii. This approach has been widely used in the literature, especially for no-load analyses.
- **Inner Rotor Modelling Approach (IRMA)** – the AFPM machine is represented by equivalent radial-flux machines with an *inner rotor* configuration.
- **Outer Rotor Modelling Approach (ORMA)** – similar to IRMA, but based on an equivalent *outer rotor* representation.

Within the scope of this thesis, the **Linear Motor Modelling Approach (LMMA)** is adopted as the reference geometric representation, while the other formulations are introduced for completeness and comparison.

These modelling approaches are schematically compared in Fig. 4.3, highlighting the conceptual reduction of the 3D AFPM problem into equivalent 2D domains.

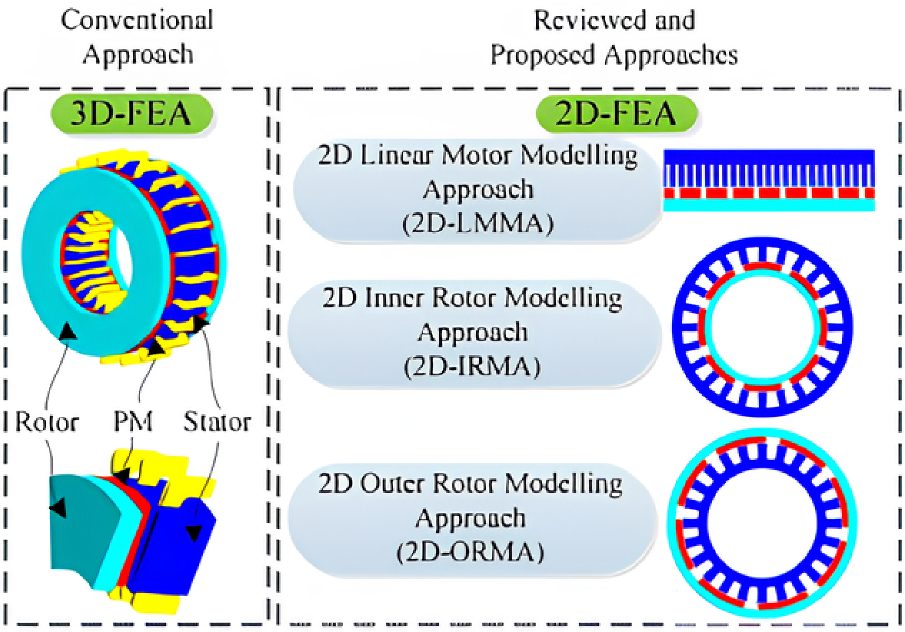

Figure 4.3: Comparison between 3D and 2D finite element modelling approaches for AFPM machines [2].

4.2 Quasi-3D approach

AFPM machines are characterized by intrinsic **three-dimensional flux paths**. As a result, the flux density distribution exhibits two distinct 3-D effects: the **curvature effect** along the radial direction and the **edge effect** along the axial direction. To accurately capture both phenomena, the use of **three-dimensional Finite Element Analysis (3-D FEA)** is generally required.

3-D FEA provides the most accurate numerical solution, since it directly solves Maxwell's equations over the discretized geometry under the specified boundary conditions. With modern FE software, the simulation of complex 3-D fields has become a standard practice. However, such simulations are often computationally expensive, requiring significant computation times. For this reason, they are not practical during the **early design stage**, when multiple design parameters must be varied across wide ranges.

To overcome these limitations, **simplified approaches** have been developed [17], such as Quasi-3D FEA and hybrid analytical–numerical models. In the Quasi-3D approach, the AFPM geometry is decomposed into several concentric cylindrical layers, each of which is "unfolded" into a 2-D planar machine model (Figure 4.4). The overall performance of the AFPM machine is then estimated by summing the contributions of the individual layers. This method captures the three-dimensional nature of AFPM machines while significantly reducing the computational burden, and it can be conveniently combined with classical FEA, analytical formulations, or reluctance network models.

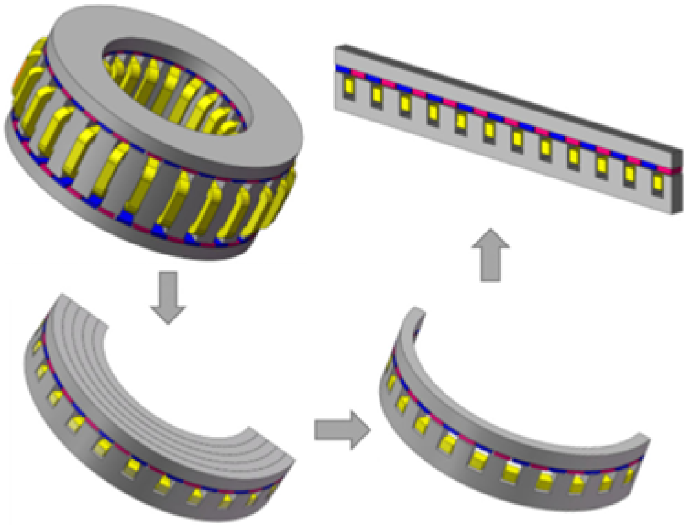

Figure 4.4: Schematic of transformation the 3D model of the AFPM machine to corresponding Q-3D and 2D models[17].

The validity of the proposed methodology has been assessed through two case studies. In the first case, the model is analyzed by means of a 2D simulation performed at the mean radius of the machine. In the second case, a Q-3D modeling strategy is adopted, based on the execution of multiple 2D simulations at four distinct radial positions, whose results are subsequently averaged in order to obtain the global machine quantities. Both analyses are implemented using the open source FEMM software [18]. The obtained results are finally compared with those derived from a high-fidelity three-dimensional reference model, the comparison includes evaluation of the magnetic flux distribution in the laminations, as well as no-load and load operating conditions. The modeling procedures and simulation results are described in detail in Chapters 5 and 6.

4.3 Comparison of Computational Efficiency

One of the major advantages of 2D FEA approaches over full 3D simulations is the drastic reduction in computation time. The study in [2] quantified these savings by comparing cogging torque simulations of AFPM motors using 3D FEA, LMMA, IRMA, and ORMA.

The results, summarized in Table 4.1, show that 3D FEA typically requires orders of magnitude longer runtimes due to the higher mesh density (up to 20 times more elements). In contrast, LMMA and IRMA can achieve similar accuracy with computational times reduced by factors ranging from 20 to over 100, depending on the case study. This makes quasi-3D 2D-based approaches particularly attractive for **parametric studies**, where a large design space must be explored.

Table 4.1: Comparison between 3D FEA and quasi-3D 2D modelling approaches for AFPM machines [2].

Approach	Back-EMF Accuracy	Torque Accuracy	Torque Ripple Prediction	Computation Time
3D FEA	Excellent (reference)	Excellent	Excellent	Very high (baseline)
2D LMMA	Very good (close to 3D)	Good	Moderate	∼20–100× faster
2D IRMA	Very good	Good	Moderate	∼50–100× faster
2D ORMA	Acceptable	Acceptable	Poor (flux leakage effects)	∼50–100× faster

It is worth noting that the computational time associated with each modeling approach strongly depends on the specific machine geometry under investigation and, most importantly, on the adopted mesh density. In general, a finer mesh leads to increased simulation time while providing higher solution accuracy. Therefore, the computation times reported in Table 4.1 should be interpreted as indicative trends rather than absolute values. In the case studies considered in this thesis, the proposed simplified models resulted in a reduction of computation time of approximately 50–60 times compared to the 3D simulations.

4.4 Discussion

The quasi-3D strategy, supported by 2D modelling approaches such as LMMA, IRMA, and ORMA, provides a **balanced trade-off** between accuracy and computational burden. While full 3D FEA remains indispensable for final design validation, the reduced-order 2D techniques enable:

- Rapid evaluation of no-load and on-load machine performance.
- Efficient parametric analysis during the preliminary design stage.
- Scalability to different AFPM topologies, including coreless machines.

According to [2], IRMA and LMMA generally provide the best compromise between speed and accuracy, whereas ORMA tends to introduce larger errors in torque ripple estimation due to flux leakage. Nevertheless, all three methods demonstrate the feasibility of reducing complex 3D AFPM problems into tractable sets of 2D FE models.

4.4.1 Concluding Remarks

The investigation by Gulec and Aydin et al [2] highlights several important findings:

- **Dual-rotor AFPM motors with symmetric magnet structures** can be effectively modelled using either LMMA or IRMA, ensuring accurate predictions with limited computational effort.
- **Motors with complex or asymmetric magnet geometries** (e.g., triangular or skewed shapes) require a higher number of 2D segments, but LMMA and IRMA still provide reliable results.
- **Coreless AFPM motors** are particularly well-suited to quasi-3D 2D modelling, since their simplified flux paths minimize non-linearities and reduce the number of required segments.
- Increasing the **pole number** generally reduces the number of required 2D slices, further lowering computational cost.
- Between the three approaches, **IRMA and LMMA** offer the best trade-off between accuracy and speed, whereas **ORMA** may be less reliable due to flux leakage effects.

In summary, quasi-3D 2D-based approaches represent a powerful and computationally efficient alternative to full 3D FEA during the **early design stages** of AFPM machines. They allow designers to perform extensive parametric studies with manageable computational resources, while reserving 3D FEA for final verification and fine-tuning of the design.

Chapter 5

FEMM Models

5.1 MATLAB–FEMM workflow and simulation driver

This chapter describes the numerical finite-element workflow adopted to generate and simulate the AFPM machine models in *Finite Element Method Magnetics* (FEMM), using MATLAB as a driver for (i) parametric geometry definition, (ii) automated pre-processing, (iii) execution of no-load and load simulations, and (iv) post-processing of the electromagnetic outputs.

The implementation is structured around a main MATLAB script that manages the overall simulation workflow, together with a set of dedicated functions for model definition and execution. The detailed workflow is illustrated in Appendix B.

The main script performs the following tasks:

1. sizing of the machine geometry and electromagnetic parameters;
2. selection of the modelling domain (full machine vs periodic sector);
3. selection of the operating condition (no-load vs on-load);
4. selection of the modelling approach (2D or quasi-3D), including the definition of the number of radial slices to be simulated in the quasi-3D case;
5. construction of structured inputs passed to the FEMM interface functions;
6. generation of the FEMM project and execution of the analysis.

5.1.1 Input data and parameterization

The AFPM model is parameterized through a set of geometric, material, and winding variables defined in the MATLAB driver. The corresponding values are summarized in Table 3.3. The main geometric dimensions include the inner and outer active diameters (D_1, D_2) and the active radial length L_c. The lamination and slot layout is described through yoke heights (h_{ys}, h_{yr}), tooth widths (w_{t1}, w_{t2}), slot width (w_s), and useful slot quantities (useful slot area A_{us} and useful height h_{us}). The air-gap and magnet parameters are set through the mechanical air-gap h_{gap}, the magnet thickness h_{pm}, and Carter's coefficient k_c.

Permanent-magnet material properties are specified by the remanent flux density B_r and relative permeability μ_r, while the stator core is characterized by the stacking factor k_{fe}. The pole and slot combination is defined by the number of poles p and the number of stator slots N_c. Finally, winding-related quantities include the number of conductors in series per phase Z_{ph}.

5.1.2 Simulation settings

The driver script sets the kinematic simulation parameters through the mechanical speed n_r (in rpm), the number of electrical periods to be simulated (M_{elec}), and the mechanical angular step $\Delta\theta_{mech}$ used to sample the rotor position during the analysis. These parameters control both the resolution of the simulated waveforms and the computational cost.

5.1.3 Full vs periodic-sector model

To reduce computational burden, the framework supports either a full-machine model or a periodic-sector model exploiting geometric periodicity. The selected option is controlled by the variable `version`:

- `full`: the complete geometry is analysed by enforcing $n_{sectors} = 1$;

- `reduced`: a periodic sector is analysed by prescribing an integer number of sectors $n_{sectors} > 1$.

The main script only enforces the user's preference; a dedicated internal validation of the admissible periodicity is delegated to the sector-based generator (flex) routine. Depending on $n_{sectors}$, the driver calls either `femm_afpm_full` (full domain) or `femm_afpm_flex` (periodic sector) Figure 5.1. The model represents only half of the machine, exploiting the electromagnetic periodicity of the AFPM topology in order to reduce the computational domain.

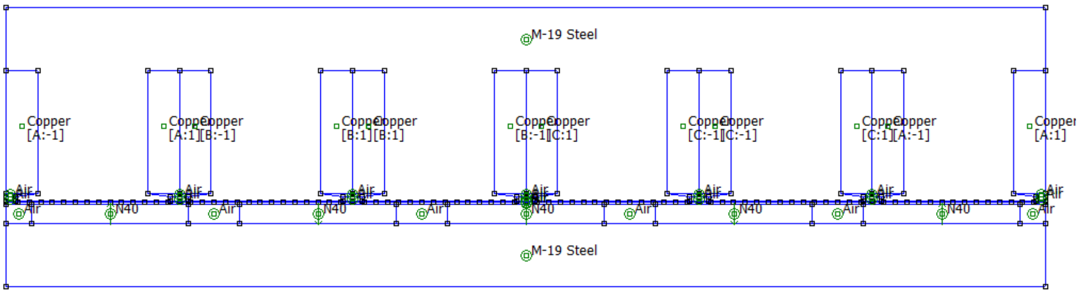

Figure 5.1: 2D Planar FEMM model.

5.1.4 Operating mode selection: no-load vs on-load

Two operating modes are supported:

- `no_load`: used to compute open-circuit electromagnetic quantities (e.g., air-gap flux distribution and phase back-EMF);
- `load`: used to compute electromagnetic torque under current excitation.

The selected mode is passed to the FEMM routines through the structured input `MOT.WDG.mode`. In load mode, the current excitation is defined in terms of *dq* components (I_d, I_q). In the present implementation, the q-axis current amplitude is determined from the slot RMS current density J_{rms} and the effective copper area A_{cu}, yielding

$$I_q = A_{cu}\, J_{rms}\, \sqrt{2}, \tag{5.1}$$

while I_d is set to zero, consistent with the surface-mounted permanent-magnet (SPM) assumption. In SPM machines the rotor exhibits negligible saliency ($L_d \approx L_q$), so the reluctance torque component is practically absent and the electromagnetic torque is mainly produced by the *q*-axis current component.

The *dq* currents are then converted into balanced three-phase currents using the inverse Park and Clarke transformations. Starting from the rotating reference frame (d, q), the transformation into the stationary $\alpha\beta$ frame is given by

$$\begin{bmatrix} i_\alpha \\ i_\beta \end{bmatrix} = \begin{bmatrix} \cos\theta_e & -\sin\theta_e \\ \sin\theta_e & \cos\theta_e \end{bmatrix} \begin{bmatrix} I_d \\ I_q \end{bmatrix}, \tag{5.2}$$

where θ_e is the electrical angle. The stationary components are then converted into three-phase currents through the inverse Clarke transformation

$$\begin{bmatrix} i_A \\ i_B \\ i_C \end{bmatrix} = \begin{bmatrix} 1 & 0 \\ -\frac{1}{2} & \frac{\sqrt{3}}{2} \\ -\frac{1}{2} & -\frac{\sqrt{3}}{2} \end{bmatrix} \begin{bmatrix} i_\alpha \\ i_\beta \end{bmatrix}. \tag{5.3}$$

The resulting phase currents are injected into the FEMM circuits `A`, `B`, and `C`. The electrical angle is defined as

$$\theta_e(t_k) = -\left(\omega_e t_k - \theta_0\right), \tag{5.4}$$

where ω_e is the electrical angular speed and θ_0 is an offset used to align the rotating current reference frame with the rotor magnetic axis.

The excitation strategy is further controlled through a flag (`invariance`) and by the electrical angle offset θ_0, which defines the phase relationship between the imposed currents and the rotor position, see Subsection 5.2.9. Two normalization options are available (`power` or `ampl`), corresponding to different invariance conventions in the Clarke transform, see Appendix C and Listing C.4.

5.1.5 Structured interface to FEMM routines

For clarity and reproducibility, the inputs are collected into two structured variables:

- `MOT.GEO`, containing the geometric and material parameters (geometry, magnets, air-gap, periodicity settings, and simulation sampling parameters);
- `MOT.WDG`, containing the winding and excitation parameters (series conductors, operating mode, current references, and electrical angle offset).

This structured interface allows the same FEMM generation and simulation routines to be reused across different case studies while keeping the main driver script compact and readable.

5.2 Sector-based FEMM model generation and simulation (`femm_afpm_flex`)

This section describes the MATLAB routine `femm_afpm_flex`, which automatically builds and simulates a 2D planar FEMM model of the AFPM machine over a reduced tangential domain exploiting periodicity. The same routine also supports on-load simulations by imposing three-phase currents derived from a prescribed *dq* reference and electrical angle offset.

5.2.1 FEMM initialization and material setup

The routine initializes a new FEMM planar document, saves the project file, and imports the required material definitions (*Air*, *Copper*, and the selected iron and PM grades). The permanent magnet material is parameterized via the coercive field H_c computed from the remanent flux density B_r and the relative permeability μ_r:

$$H_c = \frac{B_r}{\mu_0 \mu_r}. \tag{5.5}$$

Moreover, the iron lamination stacking factor k_{fe} is enforced through the FEMM lamination fill property. Three circuit properties (`A`, `B`, `C`) are finally created for phase current excitation and flux linkage extraction.

Parameter	Symbol	Value
Lamination stack coefficient	k_{fe}	0.958
PM remanence	B_r	1.08
PM relative permeability	μ_r	1.058
Permeability of free space	μ_0	$4\pi \cdot 10^{-7}$
Coercive field	H_c	$8.1232 \cdot 10^{5}$

Table 5.1: Material model parameters used in FEMM.

5.2.2 Admissible periodicity and boundary mode selection

The reduced domain is defined as one out of n_{sectors} identical tangential sectors. Since the model must be compatible with the machine symmetries, the routine validates the user-prescribed n_{sectors} against the slot number N_c and the number of pole pairs $pp = p/2$. If N_c and pp are both divisible by n_{sectors}, the requested sectoring is accepted and standard periodic boundary conditions are applied at the lateral boundaries. Otherwise, the routine enforces the minimum admissible sectoring:

- if $\gcd(N_c, pp) > 1$, the model is reduced using the minimum periodic sector $n_{\text{fix}} = \gcd(N_c, p_p)$ (periodic BC);

- if $\gcd(N_c, pp) = 1$ but $\gcd(N_c, p) > 1$, anti-periodic symmetry is used with $n_{\text{fix}} = \gcd(N_c, p)$ (anti-periodic BC);

- if neither condition holds, the routine stops since no symmetry reduction is available.

This logic ensures that the reduced model is always consistent with the electromagnetic and winding periodicity

The MATLAB implementation of this logic is reported in Appendix C, see Listing C.1.

5.2.3 Geometrical mapping to a planar tangential domain

The AFPM machine is represented by an equivalent 2D planar model, where the tangential direction is mapped onto the x-axis and the radial direction onto the y-axis. Unlike a purely averaged 2D formulation, the proposed approach adopts a slice-based quasi-3D representation, in which the machine active region is discretized along the radial direction into n_{slc} slices.

For the generic slice index slc, an equivalent diameter D_{slc} is defined as

$$D_{\text{slc}} = 2\left(\frac{D_1}{2} + \frac{\text{slc}}{n_{\text{slc}}+1}\left(\frac{D_2}{2} - \frac{D_1}{2}\right)\right), \tag{5.6}$$

which represents the radial position at which the electromagnetic quantities of the corresponding slice are evaluated. Accordingly, the pole pitch and slot pitch for each slice are computed as

$$\tau_p = \frac{\pi D_{\text{slc}}}{p}, \qquad \tau_s = \frac{\pi D_{\text{slc}}}{N_c}. \tag{5.7}$$

The reduced tangential computational domain is therefore defined as $x \in [0, x_{\text{right}}]$, with

$$x_{\text{right}} = \frac{\tau_p\, p}{n_{\text{sectors}}}, \tag{5.8}$$

where n_{sectors} denotes the number of angular sectors used in the FEMM model.

In the limiting case of a purely 2D model (i.e. $n_{\text{slc}} = 1$), the equivalent diameter reduces to the average diameter D_{avg}, thus recovering the conventional mean-radius formulation.

The FEMM problem is defined as planar, with a model depth equal to the axial core length L_c. This choice ensures that force quantities computed per unit depth by the planar solver can be directly scaled to obtain the electromagnetic torque of the machine.

The MATLAB implementation of this logic is reported in Appendix C, see Listing C.2.

5.2.4 Automated construction of rotor, magnets, air gap and stator

The routine builds the geometry by sequentially generating:

1. rotor yoke as a rectangular region (assigned to an iron material group);
2. surface-mounted magnets, repeated over the reduced number of poles $p_{\text{sec}} = p/n_{\text{sectors}}$, with alternating magnetization direction ($\pm 90^\circ$) to model north/-south polarity;
3. air regions between magnets, explicitly labelled to ensure correct material assignment;
4. stator teeth and slots through a parametric construction based on the slot opening, slot width and trapezoidal transitions;
5. stator yoke as a top rectangular iron region.

Winding regions are assigned using a dedicated procedure (`assign_windings_existing`), which labels copper blocks and maps them to the three-phase circuit definitions according to a predefined slot sequence.

5.2.5 Boundary conditions: lateral symmetry and Dirichlet closure

Three types of boundary conditions are enforced:

- lateral boundary conditions at $x = x_{\text{left}}$ and $x = x_{\text{right}}$, applied as periodic or anti-periodic constraints depending on the validated symmetry mode, where x_{left} and x_{right} denote the coordinates of the left and right boundaries of the considered computational domain;
- Dirichlet conditions on the top and bottom boundaries, used to close the magnetic domain.

To guarantee robust application of symmetry constraints across heterogeneous regions (rotor yoke, magnets, air gap subdivisions, teeth and stator yoke), the lateral boundaries are partitioned into multiple vertical segment intervals, and a dedicated periodic/anti-periodic boundary property is assigned to each interval.

5.2.6 Air gap slicing and "moving band" emulation

To emulate rotor motion within the reduced domain without explicit remeshing of a rotating part, the air gap is discretized into N tangential slices. A set of boundary properties `Airgap_1` to `Airgap_`N is created and assigned to the stator-side air-gap segments. During the simulation loop, the boundary assignment on the rotor-side air-gap segments is shifted via circular permutation, effectively reproducing a relative tangential displacement corresponding to a mechanical step $\Delta\theta_{\text{mech}}$.

Additionally, the boundary format of each air-gap slice is toggled between periodic and anti-periodic depending on how many times the slice has wrapped around the domain. This ensures consistent continuity when the shifting exceeds one sector width.

The MATLAB implementation of this logic is reported in Appendix C, see Listing C.3.

5.2.7 Simulation timeline and rotor position sampling

The simulation is performed over M_{elec} electrical periods with a mechanical angular step $\Delta\theta_{\text{mech}}$. The total simulated mechanical span is:

$$\Delta\theta_{\text{mech,tot}} = \frac{360\, M_{\text{elec}}}{p_p}, \tag{5.9}$$

and the number of simulated points is $N_1 = \lfloor \Delta\theta_{\text{mech,tot}}/\Delta\theta_{\text{mech}} \rfloor + 1$. Given the mechanical speed n_r (rpm), the mechanical angular speed is $\omega_m = 2\pi(n_r/60)$ and the electrical angular speed is $\omega_e = p_p\omega_m$. A consistent time step is computed as:

$$\Delta t = \frac{\Delta\theta_{\text{mech}}}{\omega_m}, \tag{5.10}$$

ensuring that the rotor-position sampling and the back-EMF computation are physically consistent.

5.2.8 Post-processing: flux linkage, back-EMF, and torque

For each rotor position, FEMM is solved and the following quantities are extracted:

- phase flux linkages $\lambda_A, \lambda_B, \lambda_C$ from the FEMM circuit properties Figure 5.6;
- electromagnetic torque by selecting rotor and magnet block groups and evaluating FEMM block integral #18 (force component), subsequently scaled to obtain machine torque.
- air gap flux density distribution B_g, evaluated along the air gap region to characterize the magnetic field distribution Figure 5.5.

The phase flux linkage λ_A is initially obtained from the FEMM circuit properties at each simulation step as

$$\lambda_A[k] = p_A(3), \tag{5.11}$$

where $p_A(3)$ denotes the third circuit property returned by FEMM for phase A.

Since, for modeling simplicity, the FEMM model assumes a single turn per slot, the raw flux linkage must be scaled to account for the actual number of series conductors per phase.

Let N_{turns} be the number of turns per slot of the real winding. Then, the number of turns connected in series per phase is given by

$$N_{\text{turns,ph}} = N_{\text{turns}} \cdot q \cdot pp \cdot c, \tag{5.12}$$

where q is the number of slots per pole per phase, p_p is the number of pole pairs, and c is the number of winding layers. In the present case, a double-layer winding is adopted ($c = 2$).

Each turn consists of two conductors; therefore, the total number of series conductors per phase is

$$Z_{\text{ph}} = 2\, N_{\text{turns,ph}}. \tag{5.13}$$

The phase flux linkage is then corrected as

$$\lambda_A[k] = \lambda_A[k]\, \frac{Z_{\text{ph}}}{2}\, \frac{n_{\text{sectors}} \cdot 3}{N_c}, \tag{5.14}$$

where k denotes the discrete rotor-position index of the simulation step, N_c is the total number of stator slots, and n_{sectors} is the number of periodic sectors used to represent the full machine. The scaling factors account for the number of series conductors per phase and for the extension from the reduced-sector FEMM model to the complete machine.

The phase back-EMFs are computed numerically from the flux linkages using a backward finite-difference approximation:

$$e_A[k] = \frac{\lambda_A[k+1] - \lambda_A[k]}{\Delta t}, \tag{5.15}$$

with analogous expressions for phases B and C Figure 5.7. The instantaneous torque waveform $T_e(\theta_m)$ is obtained over the simulated mechanical span, and its mean value is computed for performance evaluation Figure 5.8.

The reduced-domain results are finally scaled to represent the full machine by multiplying by the number of sectors, while the planar model depth converts force into torque. This yields a consistent full-machine torque estimate from the reduced FEMM domain.

The solution and post-processing phase of the FEMM simulations includes the evaluation of electromagnetic torque, air gap flux density profiles, and phase flux linkages. The corresponding MATLAB implementation is reported in Listing C.5. The computation of the phase back-electromotive forces from the flux linkages is subsequently performed as shown in Listing C.6.

5.2.9 Electrical angle identification from no-load flux linkage

To define a consistent electrical reference for maximum torque operation, an alignment angle is extracted from the open-circuit results. In particular, the electrical angle corresponding to the maximum of the phase A flux linkage Figure 5.2 is identified:

$$\theta_{e0} = \theta_e \left(\arg\max \lambda_A \right), \tag{5.16}$$

and converted to the corresponding mechanical angle as $\theta_{m0} = \theta_{e0}/pp$. This angle is subsequently used as an offset in the *dq*-to-*abc* transformation, so that the imposed currents are synchronized with the rotor position according to the no-load back-EMF/flux linkage reference. The resulting d–q reference frame alignment is implemented as detailed in Listing C.7.

It is worth noting that the proposed offset angle identification technique does not represent an exact determination of the optimal electrical reference, as it relies on the peak position of the no-load phase flux linkage rather than on a full electromagnetic torque maximization criterion. Nevertheless, this approach provides a reliable and computationally efficient approximation, which proves to be sufficiently accurate for the purposes of the present work. In particular, it enables a consistent *dq* reference frame alignment and yields excellent agreement in terms of back-EMF synchronization and torque prediction, while avoiding the additional complexity associated with more rigorous identification procedures.

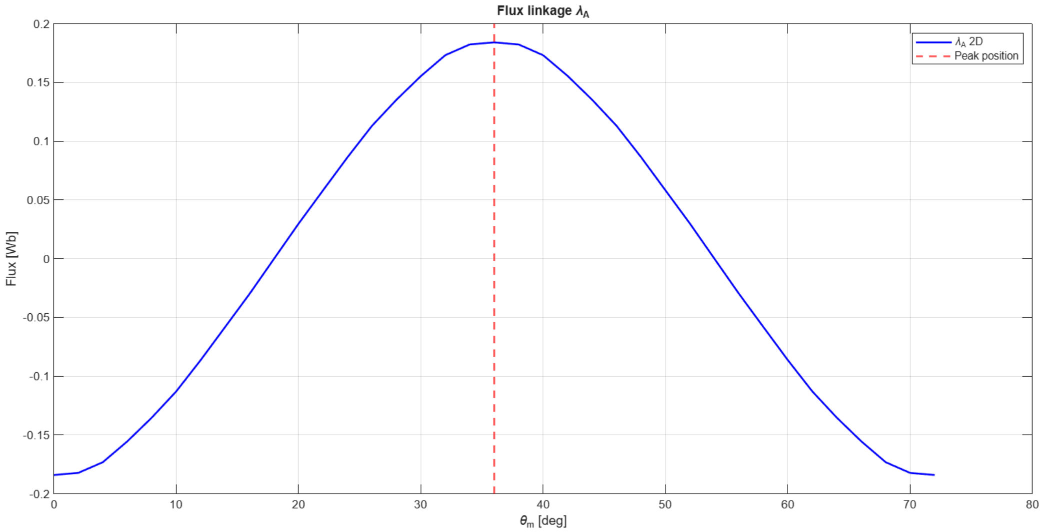

Figure 5.2: Example of no-load phase flux waveform (phase A) used to define the electrical angle reference for on-load simulations.

5.2.10 Exported data

At the end of each simulation run, the computed quantities are stored in MATLAB `.mat` files to enable systematic post-processing and comparison across operating points. For no-load simulations, the routine exports phase flux linkages, back-EMFs, electrical angle vectors, and the identified alignment angles. For load simulations, the exported dataset additionally includes the phase currents, instantaneous torque waveform, and average torque value.

5.2.11 No-load results: flux density map, flux linkage and back-EMF

No-load simulations are performed by imposing zero stator currents, so that the electromagnetic quantities are solely determined by the permanent magnets. Figure 5.3 shows the magnetic flux density magnitude map, including the color scale in Tesla. This result provides a direct indication of the peak flux density levels in teeth and back iron and allows a qualitative assessment of possible saturation regions.

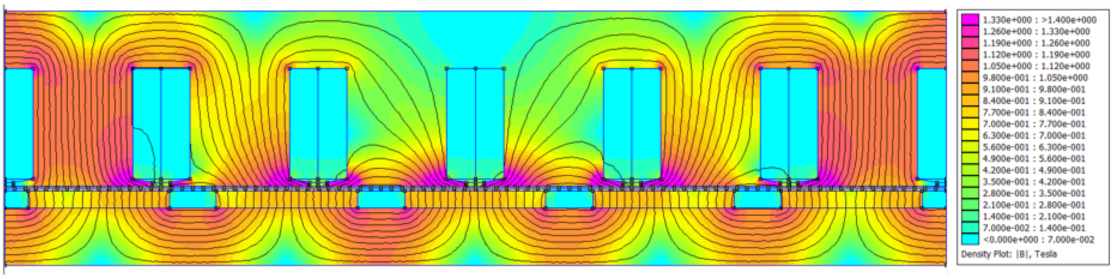

Figure 5.3: No-load magnetic flux density magnitude map **B** with color scale (T).

For completeness, an example of magnetic flux lines in the full-machine model is reported in Fig. 5.4.

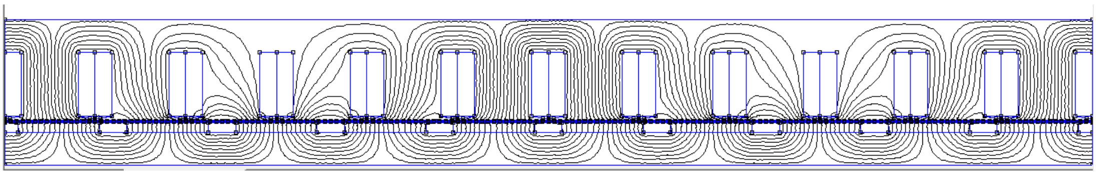

Figure 5.4: Example of magnetic flux lines in the full-machine FEMM model (no-load).

The air gap flux density profile is extracted along the air gap midline to characterize the field distribution, as shown in Fig. 5.5.

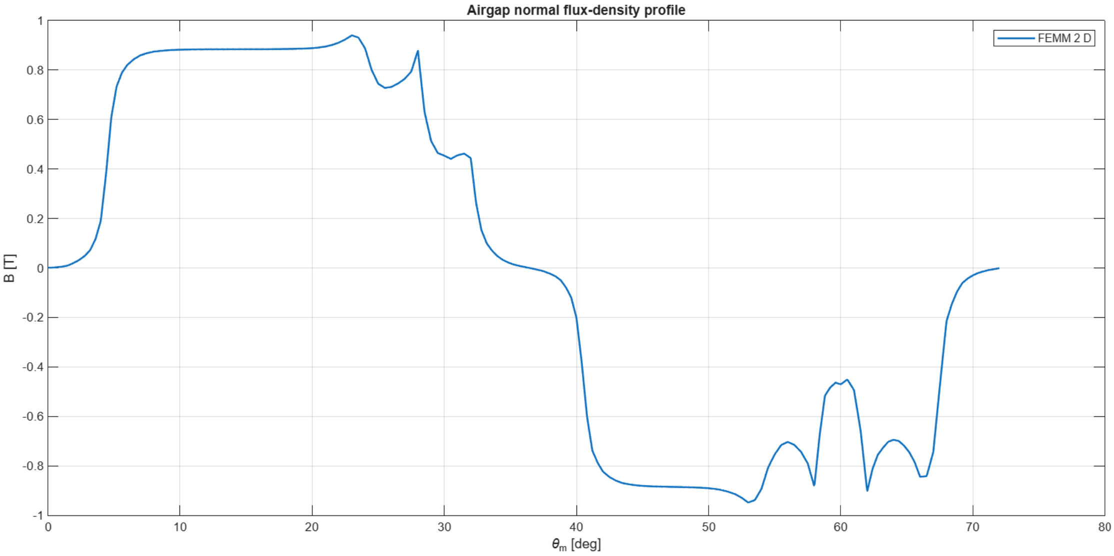

Figure 5.5: No-load air gap flux density profile B_g.

Parameter	Symbol	2D	Sizing Tool	Error [%]
Fundamental flux density	B_{g1}	0.97 T	1.04 T	-6.73

Table 5.2: Comparison of the fundamental air gap flux density obtained from the 2D FEM model and the sizing tool.

At each rotor position, the phase flux linkages are obtained from the FEMM circuit properties. Due to the single-turn assumption in the FEMM model, the raw flux linkage is scaled to account for the actual number of series conductors and to extend the reduced-sector results to the full machine, as described in Eqs. (5.12)–(5.14). The resulting no-load flux linkage waveforms are reported in Fig. 5.6.

The phase back-EMFs are then computed numerically from the flux linkages using a finite-difference approximation. The resulting back-EMF waveforms are shown in Fig. 5.7.

Parameter	Symbol	2D	Sizing Tool	Error [%]
Flux linkage peak	λ_p	0.184 Wb	–	–
Back-EMF peak	V_p	53.75 V	53.64 V	0.21

Table 5.3: Comparison between FEMM results and sizing tool predictions under no-load conditions.

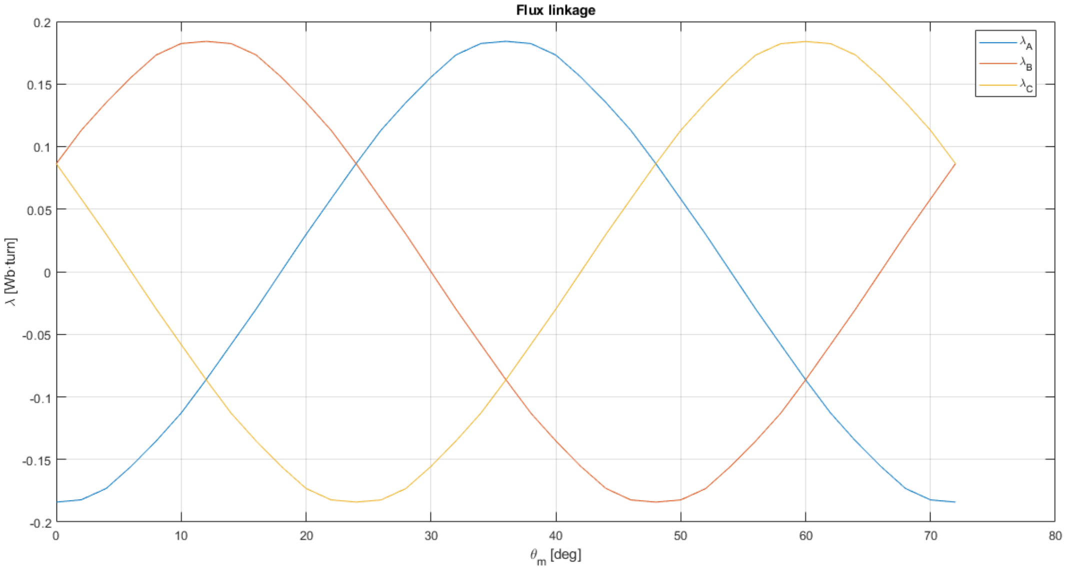

Figure 5.6: Computed phase flux linkages under no-load condition.

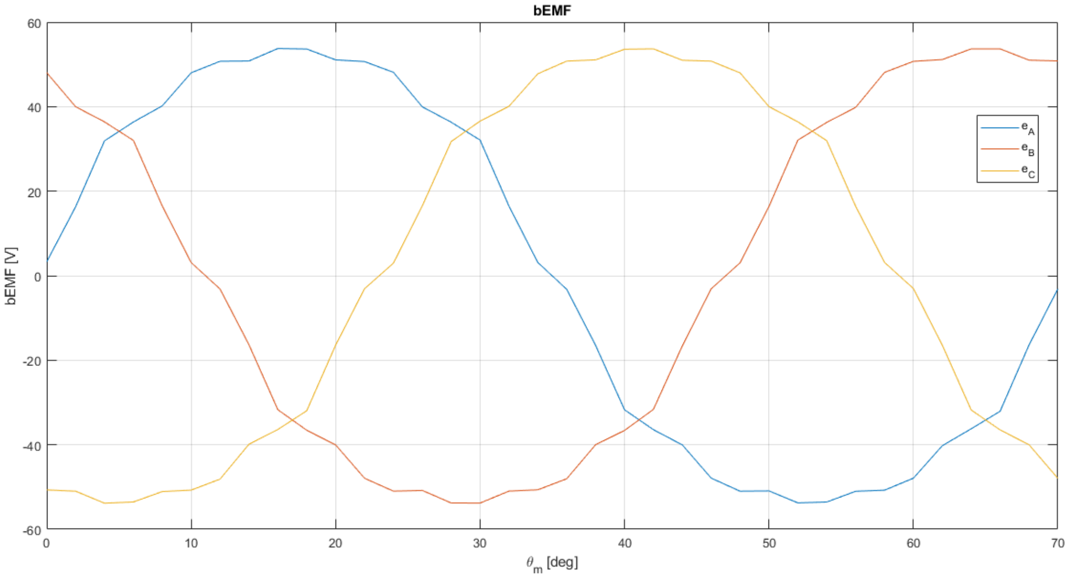

Figure 5.7: Computed phase back-EMF waveforms under no-load condition.

5.2.12 On-load results: current excitation and electromagnetic torque

On-load simulations are performed by imposing balanced three-phase currents derived from a prescribed dq reference. In the present implementation, $I_d = 0$ and the q-axis current I_q is set from the slot RMS current density and the effective copper area, as described in Section 5.1.4.

For each rotor position, FEMM is solved and the electromagnetic torque is computed by selecting the rotor and magnet groups and evaluating the corresponding FEMM block integral, subsequently scaled to obtain the full-machine torque.

The resulting instantaneous torque waveform is reported in Fig. 5.8. Its mean value is used for performance assessment, while the peak-to-peak torque ripple provides an indication of torque pulsations.

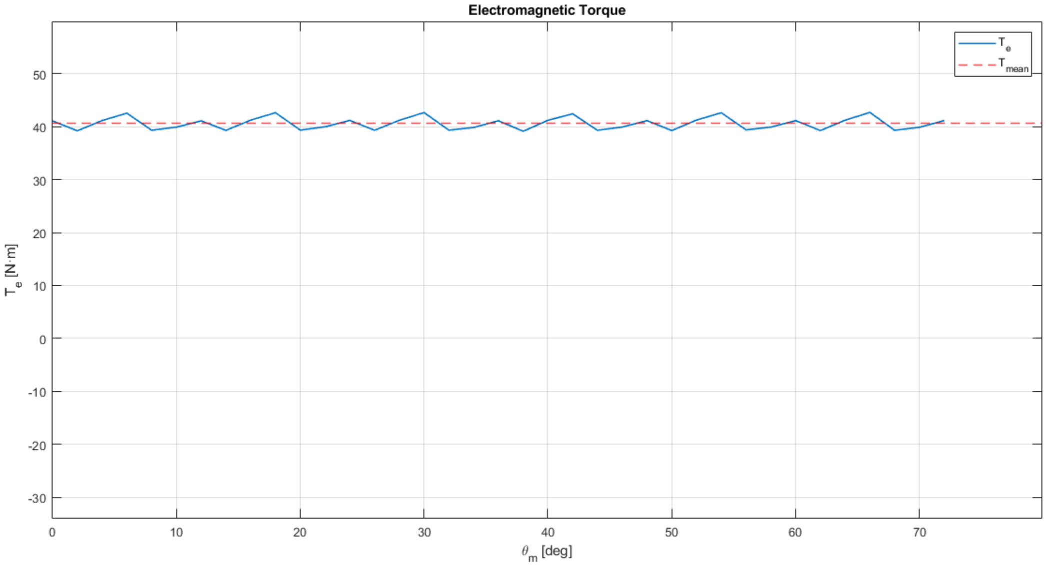

Figure 5.8: Electromagnetic torque waveform obtained from FEMM under load condition.

Parameter	Symbol	2D FEM	Sizing Tool	Error [%]
Torque peak	T_p	42.54 Nm	–	–
Torque mean	T_{ave}	40.62 Nm	40 Nm	1.55
Torque ripple	$\mathrm{TR}_{\mathrm{pp}}$	8.19 %	–	–

Table 5.4: Comparison between FEMM results and analytical predictions from the sizing tool under load conditions.

5.3 From 2D mean-radius model to quasi-3D averaging

In the baseline 2D implementation, the AFPM is represented by an equivalent 2D domain associated with a representative (mean) radius, so that the computed back-EMF and torque are interpreted as mean-radius estimates. The quasi-3D extension follows the same workflow (geometry generation, no-load back-EMF evaluation, electrical angle identification, and load simulation), repeated over multiple radii. The final machine-level quantities are then obtained by averaging the outputs across the analysed radii.

Slice	D_{avg} [mm]	λ_p [Wb]	E_p [V]
Slice 1	146.60	0.1523	43.50
Slice 2	165.20	0.1735	50.39
Slice 3	183.80	0.1945	57.02
Slice 4	202.40	0.2154	63.45
Mean Value	174.50	0.1839	53.59
2D	174.50	0.1841	53.75

Table 5.5: Quasi-3D results: per-slice outputs and aggregated quantities.

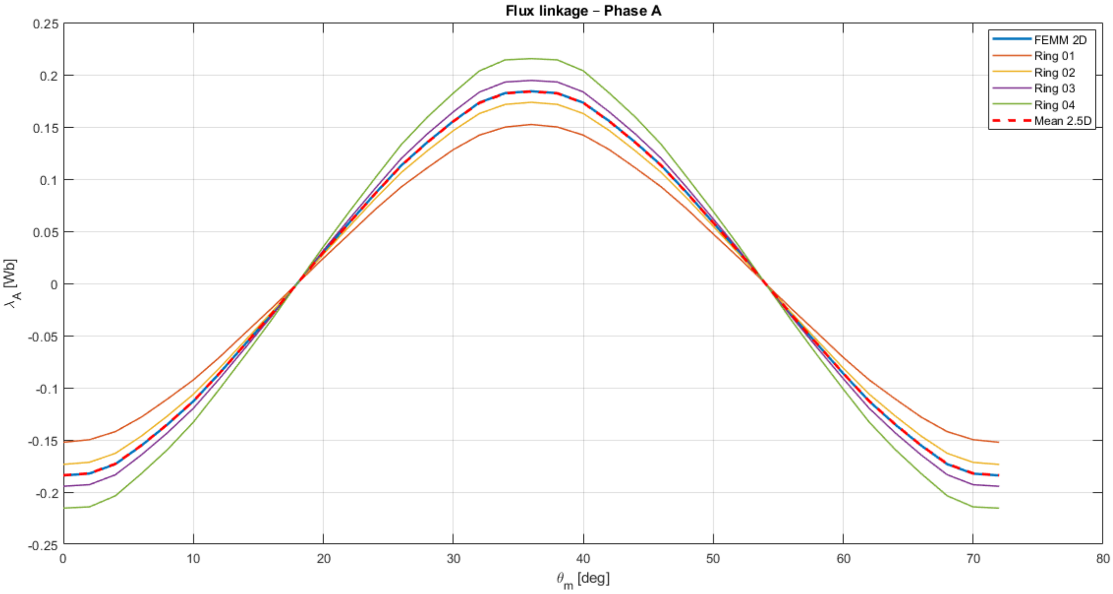

Figure 5.9: Example of no-load phase flux waveform (phase A).

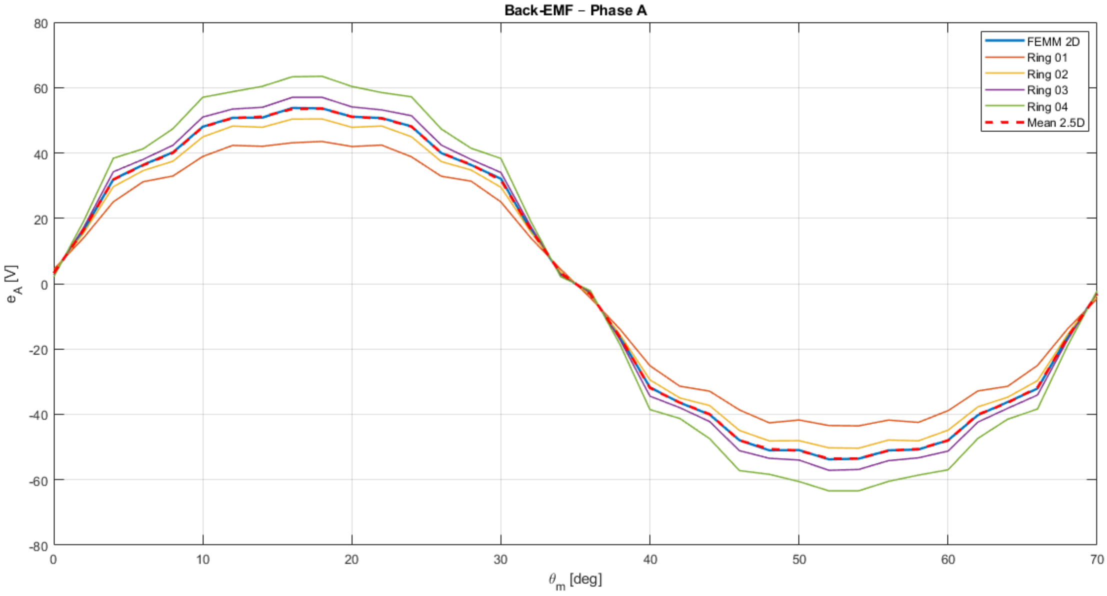

Figure 5.10: Example of b-EMF waveform (phase A).

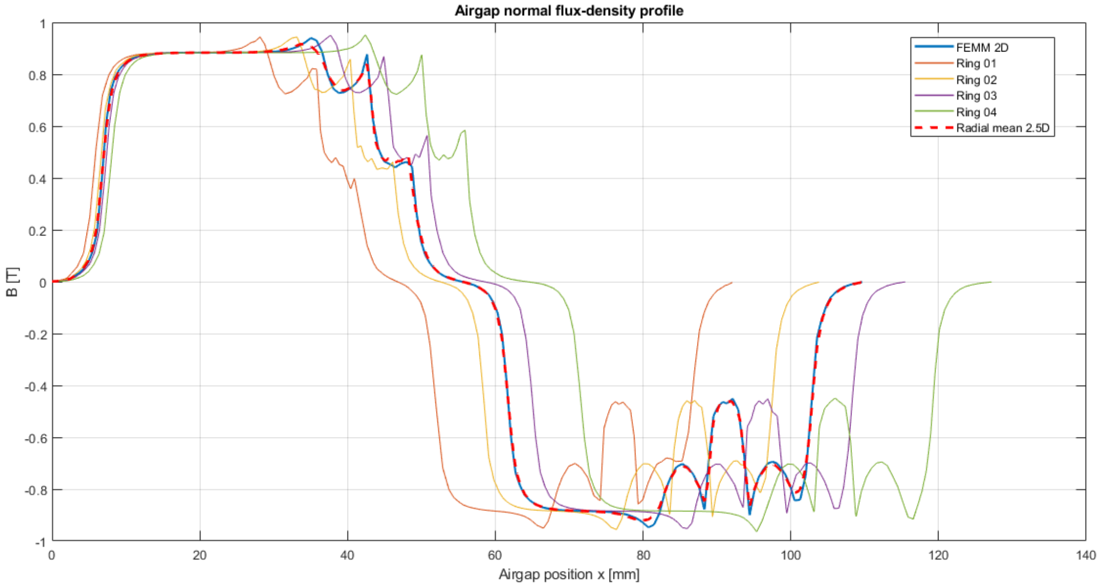

Figure 5.11: Air gap normal flux density 2D vs 2.5D.

Chapter 6

Comparison between 2D, Q-3D and 3D FEM Models

This chapter presents a comparative analysis between simplified two-dimensional (2D), quasi-three-dimensional (Q-3D or 2.5D), and full three-dimensional (3D) finite-element models of the axial-flux permanent-magnet (AFPM) machine under investigation. The 3D model is adopted as a reference solution and is taken from the work presented in [16]. The comparison is conceived as a methodological assessment aimed at evaluating the accuracy, limitations, and applicability of reduced-order models with respect to a full 3D reference formulation.

The analysis focuses on both no-load and load operating conditions, considering magnetic field distributions, air gap flux density, phase flux linkages, back-electromotive force (back-EMF), and electromagnetic torque. Particular attention is devoted to identifying the modelling assumptions that most significantly affect the prediction accuracy of each approach.

6.1 Overview of the comparison methodology

The comparison strategy adopted in this work is summarized in Fig. 6.1, which illustrates the parallel modelling workflows used for the 2D/2.5D and 3D finite-element analyses. All models are derived from the same initial AFPM design requirements and share a consistent set of geometrical, material, and electromagnetic parameters, ensuring a fair and meaningful basis for comparison.

A MATLAB-based sizing tool is employed to define the main machine parameters, which are subsequently used as inputs for both the planar and three-dimensional finite-element models. Special care is taken to ensure alignment between the different modelling approaches in terms of magnetic material properties, winding configuration, excitation conditions, and electrical reference frames.

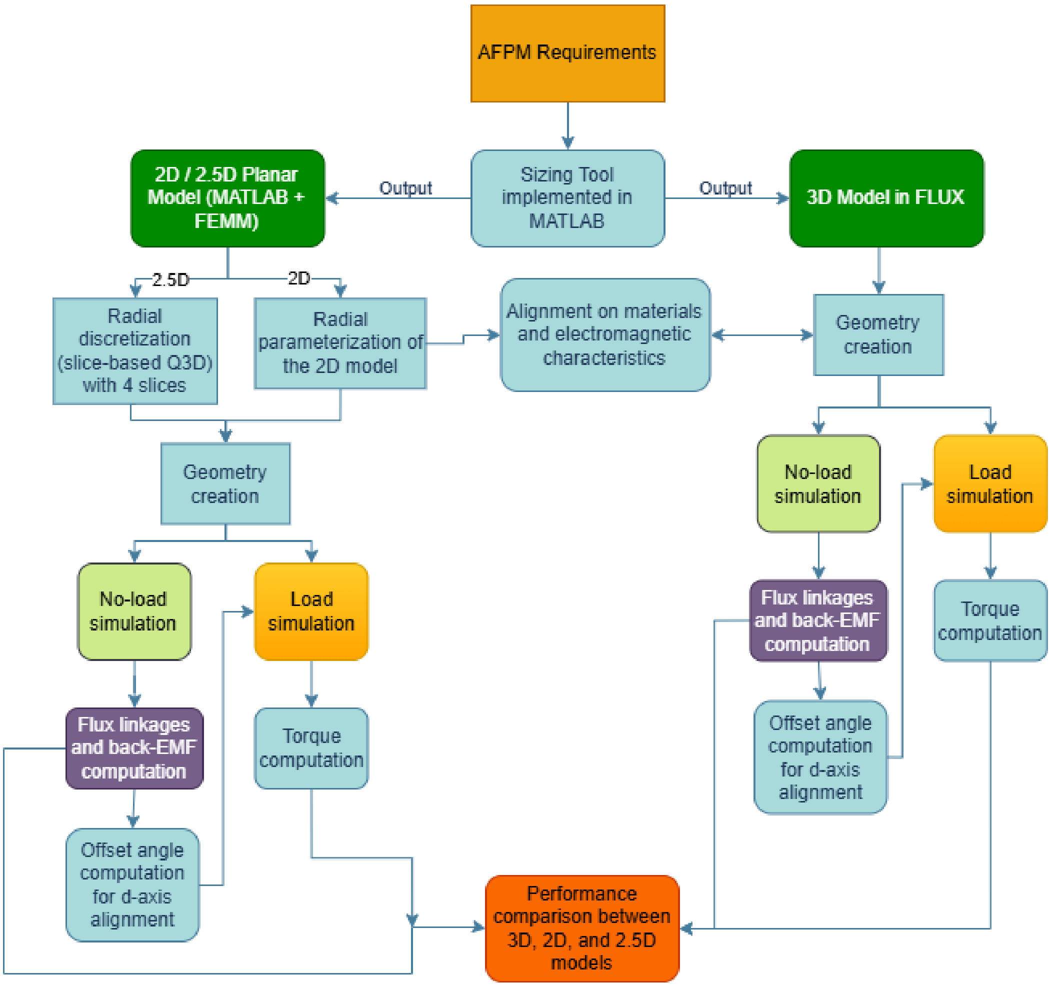

Figure 6.1: Workflow adopted for the comparison between the 2D/2.5D FEMM model and the 3D FLUX model.

6.2 Two-dimensional and quasi-3D model reference

The simplified modelling approach is based on a planar finite-element model automatically generated using MATLAB and FEMM. To account for the radial variation of the magnetic field, the machine is analysed through a quasi-three-dimensional (Q-3D or 2.5D) formulation.In this framework, the machine is discretized along the radial direction into a finite number of slices, each analysed independently using a 2D finite-element model. The global electromagnetic quantities are then reconstructed by combining the contributions of all slices through an appropriate weighting procedure.

Under no-load conditions, the 2D and Q-3D models are employed to compute magnetic flux distributions, air gap flux density, and phase back-EMF waveforms. These quantities are subsequently used to identify the electrical reference angle required for d-axis current alignment. Load simulations are then performed using the identified reference, allowing the computation of electromagnetic torque.

6.3 Three-dimensional model reference

The three-dimensional finite-element model is implemented using the commercial electromagnetic simulation software Altair Flux [19], as shown in Fig. 6.2. The full 3D model represents the complete machine geometry and is adopted as the reference solution for the comparison presented in this chapter.

The 3D modelling activity was in the master thesis work of Casalegno [16], who developed the complete geometric model and performed both no-load and load simulations within the Altair Flux environment. The simulation results obtained from the 3D model, including magnetic field distributions, back-EMF waveforms, and electromagnetic torque, were provided by him and are used in this work exclusively for comparison purposes.

Owing to its capability to explicitly account for axial flux paths, end effects, and three-dimensional magnetic interactions, the 3D model enables an accurate evaluation of electromagnetic phenomena that cannot be captured by planar formulations.

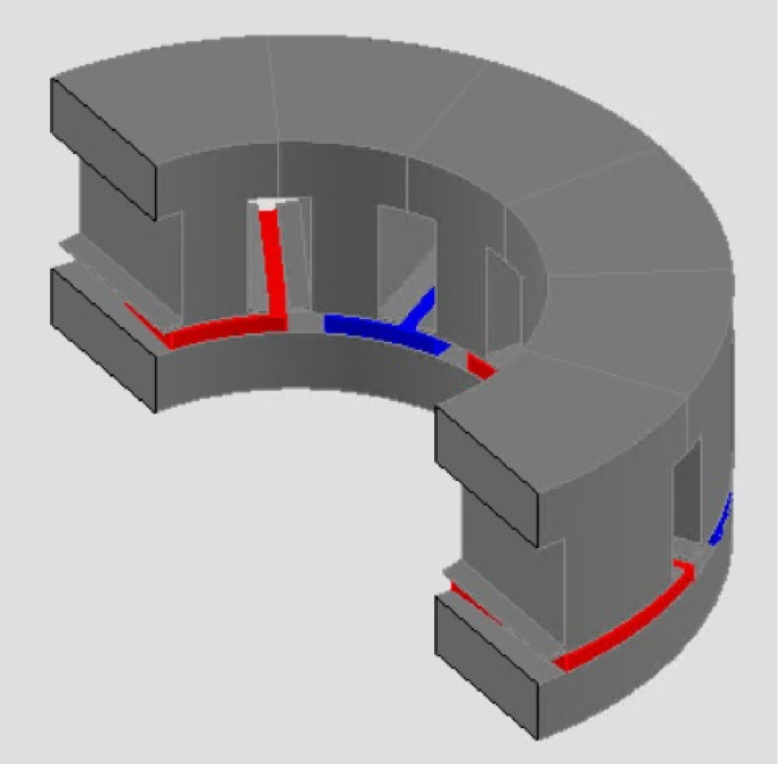

Figure 6.2: 3D FLUX model [16].

6.4 Air gap flux density comparison

The air gap flux density represents a key electromagnetic quantity, as it directly influences both the induced back-EMF and the electromagnetic torque. In this section, the air gap flux density waveforms obtained from the different modelling approaches are compared under no-load conditions.

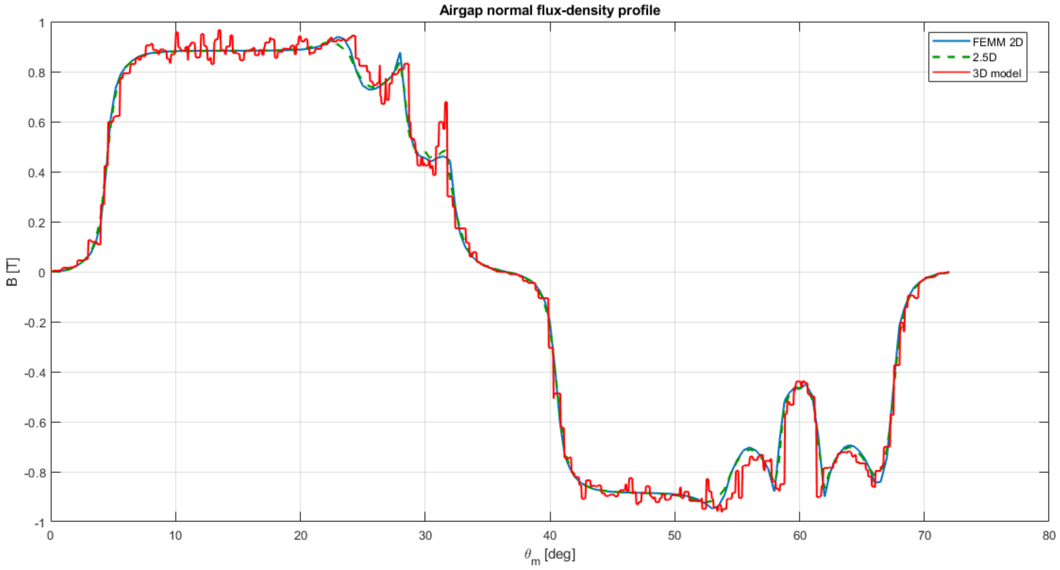

Figure 6.3: Air gap flux density waveforms under no-load conditions predicted by the 2D, Q-3D, and 3D finite-element models.

Model	**2D**	**Q-3D**	**3D**
B_{g1} [T]	0.9699	0.9691	0.9861
Relative error [%]	-1.64	-1.72	–

Table 6.1: Comparison of the fundamental air-gap flux density component B_{g1} under no-load conditions.

Figure 6.3 shows the air gap flux density waveforms predicted by the 2D, Q-3D, and 3D models. While the 2D model yields a smooth waveform representative of an averaged radial behaviour, the Q-3D approach captures the effect of radial variations, resulting in a closer agreement with the 3D reference. The 3D model exhibits additional local distortions associated with axial end effects and three-dimensional magnetic interactions.

6.5 No-load flux linkage

This section compares the magnetic flux distribution predicted by the 2D, Q-3D, and 3D finite-element models under no-load conditions.

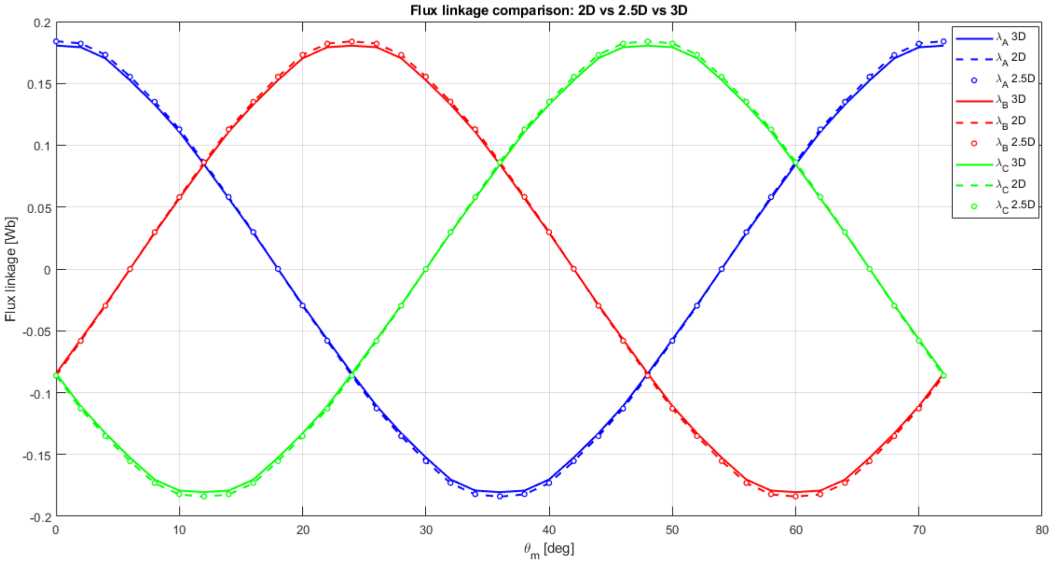

Figure 6.4: No-load magnetic flux distribution predicted by the 2D, Q-3D, and 3D finite-element models.

Model	**2D**	**Q-3D**	**3D**
λ_{peak} [Wb]	0.1841	0.1839	0.1806
Relative error [%]	1.94	1.83	–

Table 6.2: Comparison of peak phase flux linkage under no-load conditions.

The 2D model provides a simplified representation of the magnetic field, characterized by a uniform behaviour along the radial direction. The Q-3D approach introduces a spatial refinement by accounting for radial variations through the slice-based discretization. The 3D model further captures axial effects and local flux distortions that are inherently neglected in planar formulations.

6.6 Back-EMF comparison

This section presents the comparison of the phase back-electromotive force waveforms obtained from the different modelling approaches under no-load conditions.

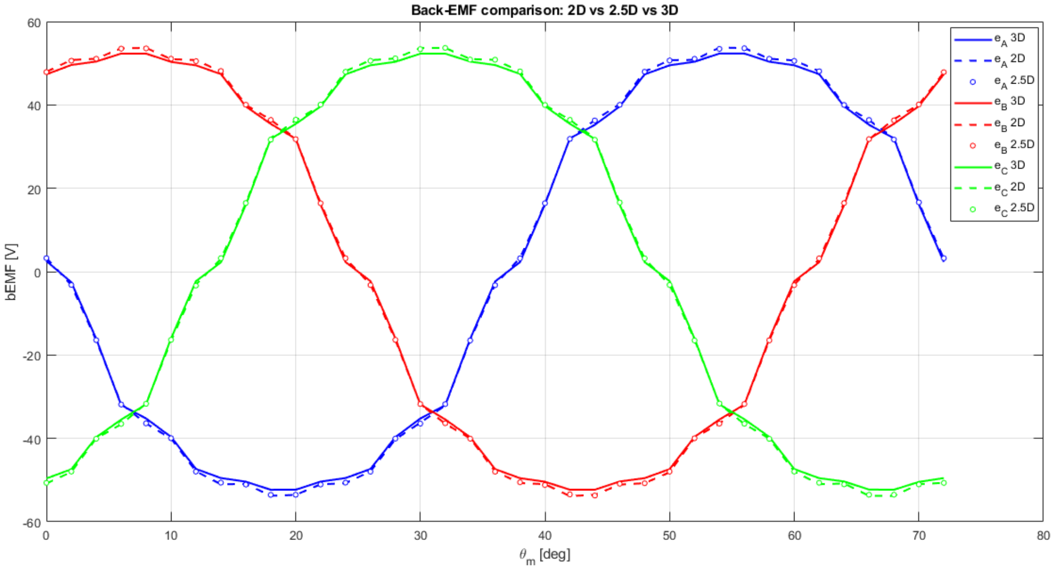

Figure 6.5: Comparison of phase back-EMF waveforms under no-load conditions predicted by the 2D, Q-3D, and 3D finite-element models.

Model	2D	Q-3D	3D
e_{peak} [V]	53.75	53.59	52.33
Relative error [%]	0.79	0.49	–

Table 6.3: Comparison of peak phase back-EMF under no-load conditions.

The back-EMF waveforms reflect the differences observed in the air gap flux density distribution. The Q-3D model provides an improved prediction of both the waveform shape and peak value when compared to the 2D formulation, while the 3D model captures additional harmonic content related to three-dimensional field effects.

6.7 Electromagnetic torque comparison

The electromagnetic torque predicted by the different models is compared under load conditions.

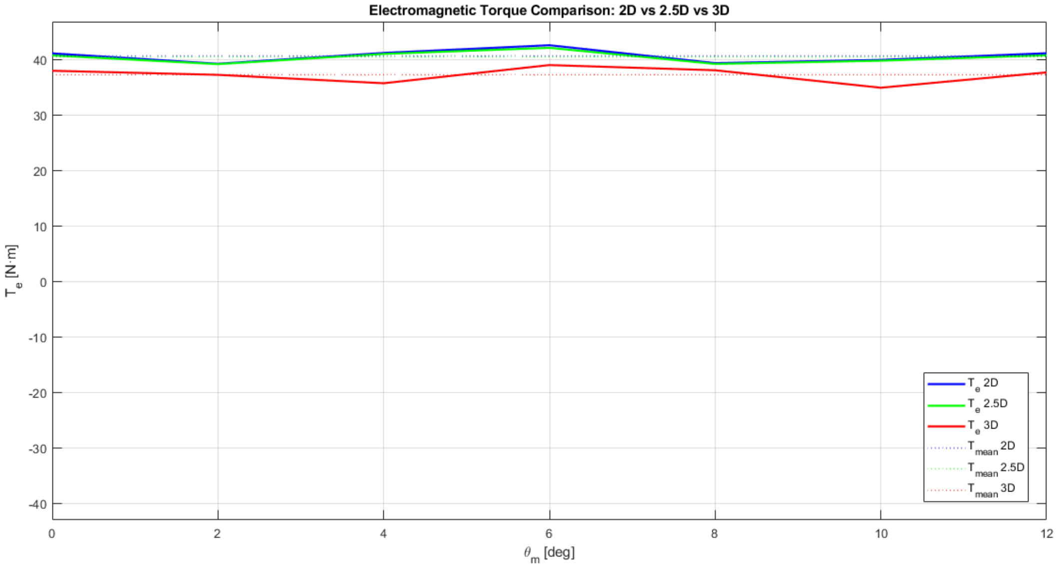

Figure 6.6: Electromagnetic torque versus mechanical angle predicted by the 2D, Q-3D, and 3D models.

Model	**2D**	**Q-3D**	**3D**
T_{mean} [Nm]	40.6	40.4	37.2
Relative error vs 3D [%]	9.14	8.60	–
Torque ripple [%]	8.2	7.3	10.9

Table 6.4: Comparison of electromagnetic torque mean value and torque ripple under load conditions between the simplified models and the 3D reference model.

6.8 Discussion and modelling trade-offs

The results of the comparison highlight the inherent trade-off between modelling accuracy and computational efficiency. While the 2D model provides rapid preliminary estimates, its accuracy is limited by the assumption of uniform radial behaviour.

The Q-3D approach represents an effective compromise, offering a significant improvement in prediction accuracy with a moderate increase in computational cost. The 3D model, although computationally demanding, remains essential for capturing three-dimensional magnetic effects and serves as a reliable reference for validation purposes.

Chapter 7

Conclusion

This thesis addressed the preliminary design and performance prediction of Axial Flux Permanent Magnet (AFPM) machines through the development of an analytical sizing procedure and the validation of simplified modelling approaches.

The objective of the work included the definition and implementation of an analytical electromagnetic sizing methodology capable of determining the main machine dimensions and equivalent circuit parameters starting from target performance specifications, material properties, and electromagnetic loading constraints. The sizing procedure provides a consistent preliminary design of the AFPM machine and allows the designer to rapidly obtain a physically meaningful geometry.

In order to validate the results obtained from the sizing procedure, simplified finite-element modelling approaches were implemented and analysed. In particular, a two-dimensional Linear Motor Modelling Approach (LMMA) and a quasi-three-dimensional (2.5D) slice-based formulation were developed and applied to the machine under investigation. The simplified models were used to evaluate the electromagnetic performance of the sized machine and were compared with a high-fidelity 3D Finite Element Analysis (FEA) reference model.

The comparison with the 3D reference model shows that the simplified approaches are capable of predicting the main electromagnetic quantities with good accuracy. In particular, the predicted electromagnetic torque differs from the reference solution by approximately 1.5–2%, while maintaining a significant reduction in computational cost. A single 2D simulation requires only a few minutes, whereas the 3D FEA model requires several hours, resulting in a computational speed-up of roughly 50–60 times.

The quasi-3D (2.5D) approach further improves the physical representation of the machine by accounting for radial variations through multiple 2D slices. However, its computational cost increases proportionally with the number of slices considered. Therefore, the number of slices must be selected as a compromise between modelling accuracy and computational efficiency.

Although the full 3D FEA model remains the most comprehensive and physically accurate approach for the analysis of AFPM machines, the results obtained in this work confirm that simplified 2D and quasi-3D models represent effective tools for the validation of analytical sizing procedures and for rapid performance estimation during the early stages of machine design.

Overall, the work demonstrates that combining an analytical sizing methodology with simplified finite-element modelling provides an efficient framework for the preliminary design of AFPM machines. The simplified models enable fast validation and parametric analysis, while the 3D model can be employed in the final stages for detailed verification and refined performance assessment.

Appendix A

MATLAB Implementation

This appendix reports two MATLAB scripts developed to implement the fast preliminary sizing procedure described in Chapter 4. The codes have been written with a modular structure in order to separate the computational core from the user interface. In this way, the main function can be reused for different case studies, while the demonstration script provides a ready-to-use example for launching the calculation.

```
% To run AFM_FastSizing.m

clear; clc;

in = struct();

% --- Target ---
in.target.T_r = 40;           % Nm
in.target.n_r = 600;          % rpm
in.target.V_r = 145;          % V_phase (phase RMS)

% --- Materials ---
in.material.k_fe = 0.958;
in.material.Br = 1.08;          % T
in.material.mu_r_pm = 1.058;
in.material.rho_cu = 1.68e-8 * 1.2358;   % ohm*m 1.724e-8
in.material.mu_env = 1.1;

% --- Limits ---
in.limits.B_ts = 1.8;          % T
in.limits.B_ys = 1.4;          % T
in.limits.B_yr = 1.4;          % T
in.limits.Ks_max = 34500;      % A/m  ( depends on cooling)
in.limits.Jrms = 7.42;            % A/mm^2

% --- Geometry ---
```

```matlab
in.geo.lambda_afm = 0.5775; %1/sqrt(3); % classic torque-oriented choice
in.geo.p  = 5;                % pole pairs
in.geo.Ns = 12;               % slots
in.geo.D_sh = 0.05;           % 50 mm
in.geo.h_gap = 1e-3;          % 1 mm
in.geo.h_pm  = 5e-3;          % 5 mm
in.geo.hgap_pm = in.geo.h_gap + in.geo.h_pm/in.material.mu_r_pm;
in.geo.alpha_pm = 0.75;       % pole-arc ratio
in.geo.k_cu = 0.307;          % copper fill factor
% slot enclosure (semi-open, square-ish)
in.geo.w_so = 5e-3;           % 5 mm
in.geo.h_ls = 1e-3;           % 1 mm
in.geo.h_es = 1e-3;           % 1 mm

% --- Winding ---
in.wind.type = 'FSCW';       % or 'DW'
in.wind.q    = (in.geo.Ns/(2*in.geo.p))/3; % slots/pole/phase (12s/10p -> q=12/(10*3)=0.4)
in.wind.nsr  = 0;            % only used for DW
in.wind.k_w1 = 0.933;        % fundamental winding factor
in.wind.k_ws = 0.933;        % back-EMF winding factor

% --- Misc / coefficients ---
in.misc.stage      = '1S1R';  % or '2S1R'
% Leakage / slot coefficients (tune for your geometry or from literature)
in.misc.sigma_gap = 0.9683;     % harmonic airgap leakage factor


% --- Solver options ---
in.opt.dDi = 0.5e-3;         % 0.5 mm step
in.opt.max_iter = 5000;

% --- Run ---
out = AFM_FastSizing(in);

% --- Display summary ---
fprintf('\n=== SUMMARY ===\n');
fprintf('Geometry: D1=%.1f mm, D2=%.1f mm, l_core=%.1f mm\n', 1e3*out.Geometry.D1,1e3*out.Geometry.D2,1e3*out.Geometry.l_core);
fprintf('Yokes: hys=%.2f mm, hyr=%.2f mm\n', 1e3*out.Geometry.hys, 1e3*out.Geometry.hyr);
fprintf('Conductors: Aus=%.2f mm^2, Acu=%.2f mm^2\n', 1e6*out.Geometry.Aus, 1e6*out.Geometry.Acu);
fprintf('Slots: wt1=%.2f mm, ws=%.2f mm, wt2=%.2f mm, hus=%.2f mm\n', 1e3*out.Geometry.wt1, 1e3*out.Geometry.ws, 1e3*out.Geometry.wt2, 1e3*out.Geometry.hus);
```

```matlab
fprintf('Flux:  Bg=%.3f T, Bg1=%.3f T\n', out.Fluxes.Bg, out.Fluxes.Bg1);
fprintf('Loads: Ks=%.0f A/m,  T e m  %.1f Nm (stage-adjusted)\n', out.Loads.Ks, out.Loads.Tem_stageAdjusted);
fprintf('Circuit: Zph=%.2f, Rs=%.3f    , Lsync=%.3e H, E0=%.1f V, Is=%.1f A', ...
     out.Circuit.Zph, out.Circuit.Rs, out.Circuit.Lsync, out.Circuit.E0, out.Circuit.Is);
```

Code A.1: demo_AFM.m

```matlab

function out = AFM_FastSizing(in)
% AFM_FastSizing       Fast preliminary sizing for Axial Flux PM motors

mu0 = 4*pi*1e-7;

% ---------- Unpack & defaults ----------
T_r  = in.target.T_r;      % Nm
n_r  = in.target.n_r;      % rpm
V_r  = in.target.V_r;      % V_phase

k_fe = in.material.k_fe;
Br   = in.material.Br;
mu_r_pm = in.material.mu_r_pm;
rho_cu  = in.material.rho_cu;
if isfield(in.material,'mu_env'); mu_env = in.material.mu_env; else, mu_env = 1.5; end

B_ts = in.limits.B_ts;
B_ys = in.limits.B_ys;
B_yr = in.limits.B_yr;
Ks_max = in.limits.Ks_max;      % A/m
Jrms_mm2 = in.limits.Jrms;      % A/mm^2
Jrms = Jrms_mm2 * 1e6;          % convert to A/m^2

lambda_afm = in.geo.lambda_afm;
p    = in.geo.p;
Ns   = in.geo.Ns;
D_sh = in.geo.D_sh;
h_gap  = in.geo.h_gap;
h_pm   = in.geo.h_pm;
hgap_pm = in.geo.hgap_pm;
alpha_pm = in.geo.alpha_pm;
k_cu = in.geo.k_cu;
w_so = in.geo.w_so;
h_ls = in.geo.h_ls;
h_es = in.geo.h_es;
```

```

wtype = in.wind.type; % ’DW’ or ’FSCW’
q     = in.wind.q;
nsr   = in.wind.nsr;       % only for DW; ignored for FSCW but keep field present
k_w1  = in.wind.k_w1;      % fundamental winding factor (torque)
k_ws  = in.wind.k_ws;      % winding factor for back-EMF

if ~isfield(in,’misc’) || ~isfield(in.misc,’stage’), stage = ’1S1R’; else, stage = in.misc.stage; end


if ~isfield(in,’opt’) || ~isfield(in.opt,’dDi’), dDi = 0.5e-3; else, dDi = in.opt.dDi; end
if ~isfield(in,’opt’) || ~isfield(in.opt,’max_iter’), max_iter = 2000; else, max_iter = in.opt.max_iter; end


% Optional leakage/slot coefficients (provide if you want accurate Lslot/Ltt)
if isfield(in,’misc’) && isfield(in.misc,’sigma_gap’), sigma_gap = in.misc.sigma_gap; else, sigma_gap = strcmpi(wtype,’FSCW’)*0.2; end

% Electrical speeds
f_r = n_r/60 * p;      % electrical frequency [Hz]
omega_e = 2*pi*f_r;    % electrical ang. speed

% Helper for stage factor on torque (approx. double for 2S1R, same for 1S1R)
stage_mul = 1;
switch upper(stage)
    case ’2S1R’, stage_mul = 2;
    otherwise,   stage_mul = 1;
end

% ---------- Iterative growth on inner diameter Di ----------
Di = D_sh;    % start from shaft diameter
iter = 0;
stop = false;
stop_reason = ’max_iter’;

while ~stop && iter < max_iter
    iter = iter + 1;

    % ---- Axial angle beta_ax (from paper eq. (4)) ----
    if strcmpi(wtype,’DW’) % DW
        beta_ax = pi/(2*p);
    else % FSCW
```

```matlab
        beta_ax = pi/Ns;
    end

    % ---- D1 from Di and beta_ax (paper eq. (5), two branches by p) ----
    if p < 6
        D1 = Di / ((1/cos(beta_ax)) - tan(beta_ax));
    else
        D1 = Di / (cos(beta_ax) - sin(beta_ax));
        % For robustness, ensure D1 > Di
        if D1 <= Di, D1 = Di + 2e-3; end
    end
    % Guard rails
    if D1 < Di, D1 = Di + 2e-3; end

    % ---- Outer diameter by lambda (eq. 6) ----
    D2 = D1 / lambda_afm;
    if D2 <= D1, D2 = D1 + 10e-3; end   % ensure positive active annulus

    % ---- Derived dimensions (eq. 7-8) ----
    De      = D2 * (sin(beta_ax) + cos(beta_ax));
    l_core = (D2 - D1)/2;
    l_PM = l_core;
    Dm      = 0.5*(D1 + D2);
    Dag     = Dm;  % airgap diameter as average, as used in inductance models

    % ---- Airgap flux density (eq. 1-3) ----
    tau_s = pi*(D1+D2)/(2*Ns);
    Kc = tau_s/(tau_s-(2*w_so/pi)*(atan(w_so/2/h_gap)-(h_gap/w_so)*log(1+(w_so/2/h_gap)^2)));
    hpm_eq  = h_pm / mu_r_pm;
    hgap_eq = Kc * h_gap;
    Bg  = Br * (hpm_eq)/(hpm_eq + hgap_eq);
    Bg1 = (4/pi) * Bg * sin(0.5*pi*alpha_pm);

    % ---- Flux per pole (eq. 9) ----
    Phi_pole  = (pi*Dm*alpha_pm*l_PM)/(2*p) * Bg;
    Phi_pole1 = (4/pi)*sin(0.5*pi*alpha_pm)*Phi_pole;  % fundamental component consistent with Bg1

    % ---- Yoke heights at D2 (eq. 10-11) ----
    num = (pi*D2*alpha_pm*Bg)/(2*p);
    hys = num / (2*B_ys*k_fe);
    hyr = num / (2*B_yr*k_fe);  % set k_fe=1 outside if rotor yoke is solid

    % ---- Teeth & slot widths (eq. 12-14) ----
```

```
    wt1 = (Bg*pi*D1/Ns) / (B_ts*k_fe);
    tau_s1 = pi*D1/Ns;
    ws  = tau_s1 - wt1;
    % at outer
    tau_s2 = pi*D2/Ns;
    wt2 = tau_s2 - ws;

    if ws <= 0
        % increase Di and continue
        Di = Di + dDi;
        continue;
    end

    % ---- Torque equation to find Acu (eq. 15) ----
    % Tem here is *single stage* analytical torque; stage multiplier applied later for check
    Tem = (sqrt(2)/16) * k_w1 * (Ns*Bg1*Jrms) * (D2^2 - D1^2) * 1 * 1; % times Acu to be solved
    % Solve for Acu s.t. Tem == T_r/stage_mul
    Acu = (T_r/stage_mul) / ( (sqrt(2)/16) * k_w1 * (Ns*Bg1*Jrms) * (D2^2 - D1^2) );

    % Slot useful area and height
    Aus = Acu / k_cu;
    hus = Aus / ws;

    % ---- Linear current density at D1 (eq. 16) ----
    Ks = k_w1 * Jrms * (Ns*Acu)/(pi*D1);   % [A/m]

    % ---- Stopping criterion (eq. 17) ----
    if Ks <= Ks_max
        stop = true;
        stop_reason = 'Ks<=Ks_max';
    else
        Di = Di + dDi;
    end
end

if ~stop
    if verbose, fprintf('[WARN] Max iterations reached without satisfying Ks<=Ks_max\n'); end
end

% Compute stage-adjusted torque for reporting
Tem_stageAdjusted = Tem * Acu * stage_mul;

% ---------------- Circuit Parameters ----------------

% Average end-winding length (eq. 20)     model choices:
```

```
% Note: the exact formulae are topology-dependent; here we reflect the paper's structure.
if strcmpi(wtype,'DW')
    lew_ave = (1 - nsr/(3*q)) * pi*(D1 + D2)/(4*p);
else % FSCW
    lew_ave = (pi*ws)/2 + (pi*(wt1+wt2))/4;
end
l_turn_ave = 2*(l_core + lew_ave);

% Conductors-in-series-per-phase Zph from closed-form (eq. 33)
% First, assemble R,L,E,I in symbolic K-forms:
% Rs = KR*Zph^2;  Lsync = KL*Zph^2;  E0 = KE*Zph;  Is = KI/Zph;

% Build K-coefficients without circular dependency:
% For generality, compute each component's coefficient with Zph factored:
% Lm_coeff, Lgap_coeff, Lslot_coeff, Lend_coeff, Ltt_coeff -> such that L = (Coeff)*Zph^2
    P = 2*p;                                         % poles
    eps_w = 1 - (P / Ns);                            % Winding pitch factor
    %gg    = 1 - (3 * eps_w / 2);                     % Leakage adjustment
    k1h   = 1 - (9 * eps_w / 16);
    k2h   = 1 - (3 * eps_w / 4);
    h_ = 0;                                          % Spacer height            (mm)
    h3        = 0;                                   % Additional height        (mm)
    lambda1 = 0;
    lambda2 = 0;
    lambda12 = 0;
    lambda_slot = 0;
    lambda_tt = 0;

   if strcmpi(wtype,'FSCW') % Concentrated winding
        lambda_slot = (k1h * (hus - h_) / (3 * ws)) + ...
                      k2h * ((h3 / ws) + (h_es / w_so) + ((h_ls / (ws - w_so)) * log(ws / w_so))) + ...
                      h_ / (4 * w_so);
        lambda_tt = (1 / (2 * pi)) * (log((hgap_pm^2 / (w_so)^2) + 0.25) + ...
                    4 * (hgap_pm / w_so) * atan(w_so  / (2 * hgap_pm)));
   else
        lambda1   = (hus / ws / 3) + 2 * h_ls / (ws + ws) + h_es / w_so;
        lambda2   = (hus / ws / 6) + 2 * h_ls / (ws + ws) + h_es / w_so;
```

```
        lambda12 = (hus / ws / 2) + 4 * h_ls / (ws + ws) + 2 * h_es / w_so;
        lambda_tt = (1 / (2 * pi)) * (log((hgap_pm^2 / w_so^2) + 0.25) + ...
                              4 * (hgap_pm / wso) * atan(w_so / (2 * hgap_pm)));
    end



% Magnetizing
if strcmpi(wtype,'DW')
    Lm_coeff = 3 * mu0 * pi * (D1 / 2 + D2 / 2) * l_core / hgap_eq * (k_ws / (pi * P))^2;  % questo già cambiato con quelli di Federica
else % FSCW
    Lm_coeff = 4 * mu0 * pi * (D1 / 2 + D2 / 2) * l_core / hgap_eq * (k_ws / (pi * P))^2;
end

% Airgap leakage
Lgap_coeff = sigma_gap * Lm_coeff;



% Slot leakage
if strcmpi(wtype,'DW')
    Lslot_coeff = mu0 * l_core /(8*P*q) * ( lambda1 + lambda2 + (2 - nsr/q)*lambda12 );
else
    Lslot_coeff = (12/Ns) * mu0 * l_core * lambda_slot;
end



% End-winding inductance
if strcmpi(wtype,'DW')
    Lend_coeff = 0.44 * mu0 * P * (q^2) * (lew_ave);
else
    Lend_coeff = mu0 * mu_env * Ns * pi * (lew_ave^2) / (12 * (q * P)^2 * hus);
end



% Tooth-tip leakage
Ltt_coeff = 12 * 3 * mu0 * l_core * k2h * lambda_tt / Ns;

% Syncronous indactance coefficient
```

```matlab
KL = Lm_coeff + Lgap_coeff + Lslot_coeff + Lend_coeff + Ltt_coeff;


% Phase resistance coefficient KR (eq. 19 -> KR multiplies Zph^2)
KR = rho_cu * (l_turn_ave)/(4*q*p*Acu);

% Back-EMF coefficient KE (eq. 30 -> proportional to Zph)
KE = 4.44 * f_r * k_ws * (Phi_pole1/2);  % E0 = 4.44 f k_ws Phi1 * (Zph/2)

% Armature current Is coefficient KI (eq. 31)
KI = (Jrms*Acu) * (Ns/3);

% Now closed-form Zph (eq. 33)
Zph = round(V_r / sqrt( (KE + KR*KI)^2 + (omega_e*KL*KI)^2 ));

% With Zph, build actual circuit parameters
Rs    = KR * Zph^2;
Lsync = KL * Zph^2;
E0    = KE * Zph;
Is    = KI / Zph;

 Lphase = KL * Zph^2;                    % Phase inductance (H)
 Lew    = Lend_coeff * Zph^2;            % End-winding inductance (H)
 Lslot  = Lslot_coeff * Zph^2;           % Slot leakage inductance (H)
 Lm     = Lm_coeff * Zph^2;              % Magnetizing inductance (H)
 Ltt = Ltt_coeff * Zph^2;                % Tooth-tip leakage inductance (H)
 Lgap = Lgap_coeff * Zph^2;              % Airgap  leakage (H)

% ---------------- Pack output ----------------
out = struct();
out.Geometry = struct('D1',D1,'D2',D2,'De',De,'l_core',l_core, ...
    'hys',hys,'hyr',hyr,'wt1',wt1,'ws',ws,'wt2',wt2,'hus',hus,'Aus',Aus,'Acu',Acu);
out.Fluxes   = struct('Bg',Bg,'Bg1',Bg1,'Phi_pole',Phi_pole,'Phi_pole1',Phi_pole1);
out.Loads    = struct('Ks',Ks,'Tem_singleStage_perAcu',Tem,'Tem_stageAdjusted',Tem_stageAdjusted);
out.Circuit  = struct('Zph',Zph,'Rs',Rs,'Lsync',Lsync,'Lm_coeff',Lm_coeff,'Lgap_coeff',Lgap_coeff, ...
    'Lslot_coeff',Lslot_coeff,'Lend_coeff',Lend_coeff,'Ltt_coeff',Ltt_coeff, ...
    'E0',E0,'Is',Is,'KR',KR,'KL',KL,'KE',KE,'KI',KI);
```

```
out.Meta      = struct('iter',iter,'stop_reason',stop_reason,'stage
    ',stage,'beta_ax',beta_ax, ...
     'Kc',Kc,'sigma_gap',sigma_gap,'lambda1',lambda1,'lambda2',
    lambda2,'lambda12',lambda12, ...
     'lambda_slot',lambda_slot,'lambda_tt',lambda_tt);
out.Induct = struct('Lphase', Lphase ,'Lew',Lew,'Lslot',Lslot,'Lm'
    ,Lm,'Ltt',Ltt,'Lgap',Lgap);

end
```

Code A.2: AFM_FastSizing.m

demo_AFM.m

This file is a demonstration script designed to provide the user with a simple way to run the sizing procedure. It defines the input structure `in`, assigning numerical values to all the necessary parameters, and then calls the main function by means of:

```
out = AFM_FastSizing(in);
```

The script can also display the main results contained in `out`. This separation between the input definition (demo script) and the computational engine (main function) ensures clarity, reproducibility, and easier modifications for further case studies.

AFM_FastSizing.m

This file contains the main function that performs the electromagnetic preliminary sizing of a surface-mounted Axial Flux Permanent Magnet (AFPM) machine. The function receives as input a structured variable `in`, which includes:

- target performance specifications (torque, speed, voltage);
- material properties (permanent magnets, lamination, copper);
- electromagnetic loading limits (flux densities, current densities);
- geometrical parameters (shaft diameter, aspect ratio, airgap length, etc.);
- winding configuration (distributed or fractional-slot concentrated).

Based on these data, the function iteratively computes the stator and rotor geometry, the flux densities, the developed electromagnetic torque, and the parameters of the equivalent circuit (resistance, inductances, back-EMF). The output is a structured variable `out` that organizes the results into dedicated subfields (`Geometry`, `Fluxes`, `Circuit`, etc.).

Appendix B

FEMM Implementation

```
clc
clear
close all

%% ===================== SETUP PATHS ==========================
addpath(fullfile(pwd, 'fun'));
addpath('C:\femm42\mfiles');

%% Geometrical Dimensions (mm)
D1      = 128;     % Inner rotor diameter
D2      = 221;     % Outer rotor diameter
Lc      = 46.5;    % Core length (radial direction)

%% Lamination Dimensions (mm)
hys     = 16.73;      % Stator yoke height
hyr     = 16.73;      % Rotor yoke height
wt1     = 16.70;      % Inner tooth width
ws      = 16.74;      % Slot width
wt2     = 41.16;      % Outer tooth width

%% Slot Area (mm )
Aus     = 537.28;     % Useful slot area
hus     = 32.10;      % Useful slot height

%% Airgap and Magnetic Dimensions
kc      = 1.2;        % Carters coefficient
hgap    = 1;          % Mechanical airgap (mm)
hpm     = 5;          % Magnet thickness (mm)

%% Electromagnetic Parameters
p       = 10;         % Number of poles
Nc      = 12;         % Number of stator slots
kfe     = 0.958;      % Iron stacking factor
```

```

%% Conductor and Magnetic Loading
Acu       = 164.94;   % Conductor cross-sectional area (mm )
alpha_pm  = 0.75;     % Pole coverage ratio (p.u.)
Br        = 1.08;     % Remanent flux density of PM (T)
mur       = 1.058;    % Relative permeability of PM material (p.u.)

%% Physical constants
mu0      = 4*pi*1e-7; % Permeability of free space          (H/m)

%% Redundant geometry (for compatibility)
wso       = 5;      % Slot opening (mm)
hls       = 1;      % Slot link height (mm)
hes       = 1;      % Slot edge height (mm)

%% Winding Parameters
Z_ph      = 246;    % Number of conductors in series per phase
N_turns   = 1;

%% Parameters of simulation
rpm       = 600;    % velocità meccanica [rpm]
M_elec    = 1;      % n. periodi elettrici da simulare
dth_mech  = 2;      % [deg meccanici] passo angolare desiderato

%% ===================== MODEL OPTIONS =========================
version   = 'reduced';      % 'full' | 'reduced'
n_sectors = 5;

dimModel  = "Q-3D";         % "2D" | "Q-3D"
n_slc        = 4;         % number of radial slices (Q-3D only)

mode      = "load";       % "load" | "no_load"
enable_B  = false;

%% ===================== CURRENTS ==============================
Jrms = 7.42;
Iq_set = Acu*Jrms*sqrt(2);  % [Aturns]
Id_set = 0;
invariance = "power";
theta0 = deg2rad(180);

%% ===================== STRUCT CREATION =======================
geo_var_list = {'D1','D2','Lc','hys','hyr','wt1','ws','wt2','Aus','hus', ...
                'kc','hgap','hpm','p','Nc','kfe','Acu','mur','mu0', ...
                'wso','hls','hes','alpha_pm','Br','n_sectors', ...
                'rpm','M_elec','dth_mech','enable_B'};
```

```matlab
MOT.GEO = create_struct('GEO', geo_var_list);

wdg_var_list = {'Z_ph','N_turns','mode','Iq_set','Id_set','invariance','theta0'};
MOT.WDG = create_struct('WDG', wdg_var_list);

%% ===================== SECTOR SELECTION ======================
switch lower(version)
    case 'full'
        MOT.GEO.n_sectors = 1;
    case 'reduced'
        MOT.GEO.n_sectors = n_sectors;
    otherwise
        error('version must be ''full'' or ''reduced''');
end

%% ============ AUTO: choose correct saved file suffix
if mode == "no_load"
    data_suffix = '_no_load_data.mat';
else
    data_suffix = '_load_data.mat';
end

%% ===================== FEMM RUN ==============================
% --- Forza n_slc = 1 nel caso 2D (così la funzione rimane la stessa) ---
if upper(string(dimModel)) == "2D"
    n_slc = 1;
end

switch upper(dimModel)

    %% ===================== 2D ================================
    case "2D"

        fprintf('\n[INFO] dimModel = 2D (mean radius model)\n');
        fprintf('[INFO] n_slc forzato = %d\n', n_slc);

        slc = 1; % unica slice

        if MOT.GEO.n_sectors == 1
            base_name = 'AFPM_2D_FULL';
            femm_afpm_full(base_name, cd, MOT, n_slc, slc);
        else
            base_name = 'AFPM_2D_SECTOR';
            femm_afpm_flex(base_name, cd, MOT, n_slc, slc);
        end

        S = load(fullfile(cd, [base_name data_suffix]));
```

```
        results = S.results;

    %% ===================== Q-3D ==============================
    case "Q-3D"

        fprintf('\n[INFO] dimModel = Q-3D | n_slc = %d radial slices\n', n_slc);

        results_sum = [];
        dt_ref = [];

        for i = 1:n_slc

            MOTi = MOT;
            tag   = sprintf('ring%02d', i);
            fname = ['AFPM_Q3D_' tag];

            % --- D_avg slice (coerente con femm_afpm_flex) ---
            Davg = 2*((D1/2) + ( (i/(n_slc+1)) * (D2/2 - D1/2) ));
            fprintf(' -> Slice %d/%d | Davg = %.3f mm | file = %s\n', i, n_slc, Davg, fname);

            slc = i;
            if MOTi.GEO.n_sectors == 1
                femm_afpm_full(fname, cd, MOTi, n_slc, slc);
            else
                femm_afpm_flex(fname, cd, MOTi, n_slc, slc);
            end

            % ---- load correct file depending on mode ----
            S  = load(fullfile(cd, [fname data_suffix]));
            ri = S.results;

            % riferimento dt
            if isempty(dt_ref)
                if isfield(ri,'dt')
                    dt_ref = ri.dt;
                else
                    error('dt non trovato nei risultati: serve dt per calcolare la b-EMF media');
                end
            end

            if i == 1
                results_sum = ri;
            else
                results_sum.lambdaA = results_sum.lambdaA + ri.lambdaA;
```

```
            results_sum.lambdaB = results_sum.lambdaB + ri.lambdaB;
            results_sum.lambdaC = results_sum.lambdaC + ri.lambdaC;


            % -> la calcolo dopo dalla lambda media (più pulito)

            if isfield(ri,'Te')
                results_sum.Te = results_sum.Te + ri.Te;
            end

            if isfield(ri,'airgap') && isfield(results_sum,'airgap')
                results_sum.airgap.Bn_profile = ...
                    results_sum.airgap.Bn_profile + ri.airgap.Bn_profile;
            end
        end
    end

    % Media semplice dei profili B
    if isfield(results_sum,'airgap')
        results_sum.airgap.Bn_profile = results_sum.airgap.Bn_profile / n_slc;
        results_sum.lambdaA = results_sum.lambdaA / n_slc;
        results_sum.lambdaB = results_sum.lambdaB / n_slc;
        results_sum.lambdaC = results_sum.lambdaC / n_slc;

        if isfield(results_sum,'Te')
            results_sum.Te = results_sum.Te / n_slc;
        end
    else
        % Anche senza airgap, faccio comunque la media delle grandezze elettriche
        results_sum.lambdaA = results_sum.lambdaA / n_slc;
        results_sum.lambdaB = results_sum.lambdaB / n_slc;
        results_sum.lambdaC = results_sum.lambdaC / n_slc;

        if isfield(results_sum,'Te')
            results_sum.Te = results_sum.Te / n_slc;
        end
    end

    % b-EMF media dalla lambda media
    results_sum.eA = diff(results_sum.lambdaA)/dt_ref;
    results_sum.eB = diff(results_sum.lambdaB)/dt_ref;
    results_sum.eC = diff(results_sum.lambdaC)/dt_ref;
```

```

        % torque mean (se disponibile)
        if isfield(results_sum,'Te')
            results_sum.T_mean = mean(results_sum.Te);
        end

        results = results_sum;
        save('AFPM_Q3D_results.mat','results');
        fprintf('[SAVE] AFPM_Q3D_results.mat\n');

    otherwise
        error('dimModel must be "2D" or "Q-3D"');
end
```

Code B.1: AFPM_main.m

Appendix C

FEMM Implementation Details

C.1 Periodicity handling

```
g  = gcd(Nc, pp);  % periodicità minima su coppie polari
g1 = gcd(Nc, p);   % periodicità minima su poli (per antisimmetria)

if mod(Nc, n_sectors) == 0 && mod(pp, n_sectors) == 0
    % Caso 1: perfettamente divisibile
    n_fix = n_sectors;
    per_mode = "periodic";
    fprintf('[OK] Il modello è divisibile per n_sectors=%d (Nc=%d, pp=%d).\n', ...
            n_sectors, Nc, pp);
else
    % Caso 2/3: non divisibile -> controllo periodicità minima
    if g > 1
        % 2a: periodicità su coppie polari
        n_fix = g;
        per_mode = "periodic";
        warning('periodicita:forzata', ...
                ['[INFO] n_sectors=%d non divide (Nc=%d, pp=%d). ', ...
                 'Uso periodicità minima n_fix=%d = gcd(Nc,pp), per_mode="%s".'], ...
                 n_sectors, Nc, pp, n_fix, per_mode);
    else
        % 2b: nessuna periodicità su coppie polari -> provo antisimmetria
        if g1 > 1
```

```
            n_fix = g1;
            per_mode = "antiperiodic";
            warning('periodicita:forzata', ...
                    ['[INFO] gcd(Nc,pp)=1. Uso antisimmetria: ', ...
                     'n_fix=%d = gcd(Nc,p)=%d, per_mode="%s".'], n_fix, g1, per_mode);
        else
            % 2c: nessuna periodicità disponibile -> STOP
            error(['[ERRORE] gcd(Nc,pp)=1 e gcd(Nc,p)=1. ', ...
                   'Nessuna periodicità individuabile: interrompo esecuzione.']);
        end
    end
end

n_sectors = n_fix;
th_sector_deg = 360 / n_sectors;

p_sec  = p  / n_sectors;
Nc_sec = Nc / n_sectors;
```

Code C.1: Periodicity calculation.

C.2 Precompute dimensions

```
% Precompute dimensions
Dslc = 2*((D1/2) + ( (slc/(n_slc+1)) *(D2/2-D1/2) ) );

pole_pitch = pi * Dslc / p;
slot_pitch = pi * Dslc / Nc;

hgap = hgap+hgap/2; % to have the 2 airgap equal to hgap/2


% FEMM problem definition
mi_probdef(0, 'millimeters', 'planar', 1e-8, Lc, 30, 0);
```

Code C.2: Precompute dimensions.

C.3 Air gap moving band

```

y1 = y_airgap_line1;
y2 = y_airgap_line2;
```

```
bnd_names = compose('Airgap_%d', (1:b));

% Creazione segmenti di divisione airgap
j=1;
for a = 0 : s : (Lx_red - s)
    bnd_name = sprintf('Airgap_%d', j);
    mi_addboundprop(bnd_name, 0,0,0,0,0,0,0,0, 4);
    mi_addnode(a, y1);
    mi_addnode(a+s , y1);
    mi_addsegment(a, y1, a+s, y1);

    mi_addnode(a, y2);
    mi_addnode(a+s , y2);
    mi_addsegment(a, y2, a+s, y2);
    mi_selectsegment(a+s/2, y2);
    mi_setsegmentprop(bnd_name, 1, 0, 0, grp_airgap_stator);
    mi_clearselected();
    j= j+1;
end

bnd = cellstr(bnd_names(:)).';
NA  = numel(bnd);
wrapCount = zeros(1, NA);

for k = 1:N1
    for j = 1:NA
        if mod(wrapCount(j), 2) == 0
            mi_modifyboundprop(bnd{j}, 9, 4);
        else
            mi_modifyboundprop(bnd{j}, 9, 5);
        end
    end

    for j = 1:NA
        a = (j-1)*s;
        mi_clearselected();
        mi_selectsegment(a + s/2, y1);
        mi_setsegmentprop(bnd{j}, 1, 0, 0, grp_airgap_rotor);
        mi_clearselected();
    end

    bnd       = circshift(bnd, [0, 1]);
    wrapCount = circshift(wrapCount, [0, 1]);
    wrapCount(1) = wrapCount(1) + 1;
end
```

Code C.3: Air gap moving band.

C.4 Current excitation: load vs no-load

```
if sim_mode == "load"

    if k == 1
        fprintf(">>> ENTRO NEL RAMO LOAD\n");
    end

    % tempo dello step k (coerente con dt)
    t_k = (k-1)*dt;                       % [s]

    % angolo elettrico con offset d--q
    theta_e = -( we * t_k - theta0);      % [rad]

    % correnti dq (costanti nel punto di lavoro)
    Id = Id_set;
    Iq = Iq_set;

    % dq -> alpha-beta (Park inversa)
    ct = cos(theta_e);
    st = sin(theta_e);
    ialpha =  ct*Id - st*Iq;
    ibeta  =  st*Id + ct*Iq;

    % alpha-beta -> abc (Clarke inversa)
    switch lower(invariance)
        case "power"
            IA(k) =  (ialpha);
            IB(k) = (-0.5*ialpha + (sqrt(3)/2)*ibeta);
            IC(k) = (-0.5*ialpha - (sqrt(3)/2)*ibeta);
        case "ampl"
            k_cl = sqrt(2/3);
            IA(k) =  k_cl*(ialpha);
            IB(k) =  k_cl*(-0.5*ialpha + (sqrt(3)/2)*ibeta);
            IC(k) =  k_cl*(-0.5*ialpha - (sqrt(3)/2)*ibeta);
        otherwise
            error('invariance must be ''power'' or ''ampl''');
    end

    % impongo la corrente nei circuiti A, B, C
    mi_setcurrent('A', IA(k));
    mi_setcurrent('B', IB(k));
    mi_setcurrent('C', IC(k));

else
    if k == 1
        fprintf(">>> ENTRO NEL RAMO NO_LOAD\n");
    end
```

```

    IA(k) = 0;
    IB(k) = 0;
    IC(k) = 0;

    % impongo la corrente nei circuiti A, B, C
    mi_setcurrent('A', IA(k));
    mi_setcurrent('B', IB(k));
    mi_setcurrent('C', IC(k));
end
```

Code C.4: Phase current assignment in load and no-load simulations.

C.5 Solve and post-processing

```
% solve -> read B -> read lambda and F

% 4) Solve e post-processing
mi_analyze(0);
mi_loadsolution;

% COPPIA FEMM via mo_blockintegral(18)
% Seleziono i blocchi del rotore e dei magneti
mo_clearblock();
mo_groupselectblock(grp_rotor);    % gruppo 2
mo_groupselectblock(grp_magnet);   % gruppo 3

Fx = mo_blockintegral(18);         % [N]

% Scala per profondità del modello e periodicità (n_sectors)
Te(k) = Fx * n_sectors * Lc*1e-3;    % [N m]

mo_clearblock();

% AIR-GAP B: campionamento profilo spaziale a metà traferro
if enable_airgapB && k==1
    for ii = 1:N_Bpts
        vals = mo_getpointvalues(x_B(ii), y_midgap);  % [A, Bx, By
    , ...]
        by = vals(3);
        Bn_profile(k, ii) = by;    % normale ("B nel traferro")
    end
end

pA = mo_getcircuitproperties('A');    % [I, V, lambda]
pB = mo_getcircuitproperties('B');
pC = mo_getcircuitproperties('C');
```

```

% Flux linkage
lambdaA(k) = pA(3);
lambdaB(k) = pB(3);
lambdaC(k) = pC(3);

lambdaA(k) = lambdaA(k)*(Zph/2)*(n_sectors*3/Nc);
lambdaB(k) = lambdaB(k)*(Zph/2)*(n_sectors*3/Nc);
lambdaC(k) = lambdaC(k)*(Zph/2)*(n_sectors*3/Nc);

% Barra
elapsed = toc(t0);
eta = elapsed*(N1/k - 1);
waitbar(k/N1, hwb, sprintf('TIME: %3.0f%% | elapsed %.1fs | ETA %.1fs', ...
        100*k/N1, elapsed, eta));
```

Code C.5: FEMM solve and post-processing: torque, air gap flux density sampling, flux linkages, and back-EMF.

```
% --- bEMF ---
eA = diff(lambdaA)/dt;
eB = diff(lambdaB)/dt;
eC = diff(lambdaC)/dt;
```

Code C.6: Back-EMF computation from flux linkages.

C.6 d–q axis alignment

```
%% === Stima offset assi d--q dalla BEMF/lambda ===
% Picco della lambdaA
[~, kmax] = max(lambdaA);

% ELETTRICO:
theta_e0_deg = theta_e_deg(kmax);

% MECCANICO:
theta_m0_deg = theta_e0_deg / pp;

fprintf('[DQ align lambda] theta_e0=%.2f deg (from lambdaA) | theta_m0=%.2f deg\n', ...
        theta_e0_deg, theta_m0_deg);
```

Code C.7: Estimation of the d–q axis offset from the phase flux linkage.

Bibliography

[1] Matías Jiménez Molina, Federica Graffeo, Silvio Vaschetto, Alberto Tenconi, and Andrea Cavagnino. «Fast Procedure for the Electromagnetic Sizing of Axial Flux PM Motors». In: *2024 International Conference on Electrical Machines (ICEM)*. Torino, Italy: IEEE, Sept. 2024, pp. 1–6. DOI: `10.1109/ICEM60801.2024.10700359` (cit. on pp. 1, 17, 20, 22, 27).

[2] Mehmet Gulec and Metin Aydin. «Implementation of different 2D finite element modelling approaches in axial flux permanent magnet disc machines». In: *IET Electric Power Applications* 12.2 (2018), pp. 195–202. DOI: `10.1049/iet-epa.2017.0434` (cit. on pp. 1, 35–38, 40, 41).

[3] Juha Pyrhönen, Tapani Jokinen, and Valéria Hrabovcová. *Design of Rotating Electrical Machines*. John Wiley & Sons, 2008. ISBN: 978-0-470-69516-6 (cit. on pp. 3, 6).

[4] Austin Hughes and Bill Drury. *Electric Motors and Drives: Fundamentals, Types and Applications*. 6th. Butterworth-Heinemann, 2019. ISBN: 978-0-08-102615-1 (cit. on p. 4).

[5] Jorge Luis Lora. «Design and Multi-Objective Optimisation of the Axial Flux Machine». Master's thesis. Politecnico di Torino, 2023/2024 (cit. on p. 6).

[6] Z. Hao, Y. Ma, P. Wang, G. Luo, and Y. Chen. «A Review of Axial-Flux Permanent-Magnet Motors: Topological Structures, Design, Optimization and Control Techniques». In: *Machines* 10.12 (Dec. 2022), p. 1178. DOI: `10.3390/machines10121178`. URL: `https://doi.org/10.3390/machines10121178` (cit. on pp. 8, 11, 12).

[7] Amin Mahmoudi, N. A. Rahim, and W. P. Hew. «Axial-flux permanent-magnet machine modeling, design, simulation, and analysis». In: *Scientific Research and Essays* 6.12 (June 2011), pp. 2525–2549. ISSN: 1992-2248 (cit. on pp. 10, 12–14).

[8] Q. Wang, X. Zhang, Y. Li, et al. «Novel Double-Sided Stator Single-Rotor Axial Flux Permanent Magnet Motor». In: *World Electric Vehicle Journal* 13.3 (2022), p. 52. DOI: `10.3390/wevj13030052` (cit. on p. 11).

[9] J. F. Gieras, R. J. Wang, and M. J. Kamper. *Axial Flux Permanent Magnet Brushless Machines.* Springer, 2008 (cit. on pp. 11, 12).

[10] A. Parviainen. «Design of Axial Flux Permanent Magnet Low-Speed Machines and Performance Comparison Between Radial Flux and Axial Flux Machines». In: *Acta Universitatis Lappeenrantaensis* (2005) (cit. on p. 12).

[11] Ayman M. El-Refaie, Thomas M. Jahns, and Donald W. Novotny. «Analysis of Surface Permanent Magnet Machines with Fractional-Slot Concentrated Windings». In: *IEEE Transactions on Energy Conversion* 21.1 (2006), pp. 34–43 (cit. on p. 16).

[12] S. Vaschetto, A. Tenconi, and G. Bramerdorfer. «Sizing procedure of surface mounted PM machines for fast analytical evaluations». In: *2017 IEEE International Electric Machines and Drives Conference (IEMDC).* IEEE, 2017, pp. 1–8. DOI: `10.1109/IEMDC.2017.8002096` (cit. on p. 17).

[13] Thomas A. Lipo. *Introduction to AC Machine Design.* Hoboken, NJ: Wiley, 2017 (cit. on pp. 19, 22).

[14] Juha Pyrhönen, Tapani Jokinen, and Valeria Hrabovcová. *Design of Rotating Electrical Machines.* Wiley, 2014 (cit. on p. 19).

[15] Paul Campbell. «Principles of a Permanent-Magnet Axial-Field D.C. Machine». In: *Proceedings of the IEEE* 121.12 (1974), pp. 1519–1525 (cit. on p. 21).

[16] Emanuele Casalegno. «Design and Finite Element Analysis of Permanent Magnet Axial Flux Machines». M.Sc. thesis. Turin, Italy: Politecnico di Torino, Mar. 2026 (cit. on pp. 35, 58, 60, 61).

[17] T. Zou, D. Li, R. Qu, J. Li, and D. Jiang. «Analysis of a Dual-Rotor, Toroidal Winding, Axial-Flux Vernier Permanent Magnet Machine». In: *IEEE Transactions on Industry Applications* 53.3 (May 2017), pp. 1920–1930. DOI: `10.1109/TIA.2017.2655004` (cit. on p. 39).

[18] David Meeker. *Finite Element Method Magnetics (FEMM).* Version 4.2, Accessed: 2025-03-01. 2022. URL: `http://www.femm.info` (cit. on p. 39).

[19] Altair Engineering Inc. *Altair Flux: Electromagnetic Field Simulation Software.* Available at: https://altair.com/flux. Altair Engineering. Troy, MI, USA, 2024 (cit. on p. 60).